

Dense water downslope flow and AABW production in a numerical model: Sensitivity to horizontal and vertical resolution in the region off Cape Darnley polynya



Vigan Mensah^{a,*}, Yoshihiro Nakayama^a, Masakazu Fujii^b, Yoshifumi Nogi^b, Kay I. Ohshima^a

^a Institute of Low Temperature Science, Hokkaido University, Sapporo, Japan

^b National Institute of Polar Research, Tachikawa, Japan

ARTICLE INFO

Keywords:

Ocean-ice modeling
Ocean general circulation models
(OGCM)/regional ocean models
Polynyas
Dense water production
Downslope flow
East antarctica

ABSTRACT

The formation of Dense Shelf Water (DSW) and Antarctic Bottom Water (AABW) in the Southern Ocean is an essential part of the thermohaline circulation, and understanding this phenomenon is crucial for studying the global climate. AABW is formed as DSW flows down the continental slope and mixes with the surrounding waters. However, DSW formation and its descent remains a poorly resolved issue in many ocean models. We, therefore, simulated the formation and descent of DSW and investigated the model sensitivities to horizontal and vertical grid spacings. The Massachusetts Institute of Technology general circulation model (MITgcm) was used for the region off Cape Darnley in East Antarctica, one of the main AABW production areas, where historical and mooring data are available for comparison. Simulations with coarse horizontal grid resolutions of order (10 km) yielded high volumes of DSW on the shelf. However, the largest part of this DSW was transformed into intermediate water and advected westward. Horizontal model resolutions equal to or higher than 2 km were required to simulate the descent of DSW and a realistic AABW production. Simulated time series at a mooring located at a depth of 2,600 m showed periodic fluctuations in velocity and temperature of 0.3 m s^{-1} and $0.5 \text{ }^{\circ}\text{C}$, respectively, consistent with observations. We also found that high-resolution bathymetry datasets are crucial because the newly formed AABW volume was reduced by 20% when a smoother bathymetry was used on a 2-km resolution grid. Vertical resolution had little influence on model performance because the plume was much thicker ($> 170 \text{ m}$) than the grids width. Therefore, reproducing the downslope flow of DSW and AABW formation in the Cape Darnley region can be achieved with a high horizontal resolution ($\leq 2 \text{ km}$) and a relatively coarse vertical resolution ($\sim 100 \text{ m}$ on the continental slope).

1. Introduction

Antarctic Bottom Water (AABW) is an essential water mass that occupies the bottom of all global oceanic basins (Ferreira and Kerr, 2017; Johnson, 2008). AABW formation is a major driver of deep global overturning circulation (Lumpkin and Speer, 2007; Talley, 2013); and as such, it affects the global climate (Abrahamsen et al., 2019; Kerr et al., 2018; Orsi et al., 1999; Purkey and Johnson, 2010, 2013; Schmitz, 1995). Understanding and modeling the formation and properties of AABW and how these vary is therefore a crucial topic in climate-related studies.

AABW is formed as a result of the downslope flow of Dense Shelf Water (DSW) along the continental slope and the mixing of this descending DSW with other water masses (Bindoff et al., 2000; Orsi et al., 1999; Rodman and Gordon, 1982). DSW – also called High Salinity Shelf Water – is a cold, salty, and dense water mass formed in winter mainly in coastal polynyas at several locations around Antarctica

(Markus et al., 1998; Morales Maqueda et al., 2004; Renfrew et al., 2002; Williams et al., 2010). When sea ice forms in winter, brine rejection occurs, and the salinity of the cold surface waters increases. The water becomes denser and sinks towards the bottom over the continental shelf then flows down the continental slope via troughs and underwater canyons (Baines and Condie, 1998; Gordon et al., 2009). AABW is formed as DSW flows deeper and mixes with surrounding waters, mainly modified Circumpolar Deep Water (mCDW) or Warm Deep Water (Foster and Carmack, 1976; Gill, 1973; Nicholls et al., 2009; Whitworth III et al., 1998). The Ross Sea, Weddell Sea, the region off the Adélie coast, and the region off Cape Darnley are the known sites for DSW production and AABW formation (Fukamachi et al., 2000; Gordon et al., 1993; Jacobs et al., 1970; Ohshima et al., 2013; Rintoul, 1998; Williams et al., 2010). AABW may also be formed in a similar way following the downslope flow of Ice Shelf Water, a water mass resulting from the cooling of waters flowing beneath an ice shelf (Foldvik et al., 1985).

* Corresponding author.

E-mail address: vmensah@lowtem.hokudai.ac.jp (V. Mensah).

Modeling AABW formation is challenging, and previous studies raised many issues requiring further investigations (Downes et al., 2011; Dutay et al., 2002; England, 1992; Kerr et al., 2009; Kim and Stössel, 1998; Renner et al., 2009; Sasai et al., 2004; Stössel et al., 1998; Treguier et al., 2010). In many global climate models with coarse horizontal resolutions (coarser than ~ 20 km), AABW is formed more as a result of deep ocean convection in the open-ocean regions rather than sea ice formation on the shelf (e.g., Goosse et al., 2001; Heuzé et al., 2013; Stössel et al., 1998; Kiss et al., 2020). Modeled AABW formation through this inaccurate process yields unrealistic AABW properties (Azaneu et al., 2014). Another crucial issue lies in DSW pathways (e.g., Van Sebille et al., 2013). Many global ocean circulation models successfully reproduce DSW formation on the shelf but cannot reproduce its flow down the continental slope (e.g., Rodehacke et al., 2007). In particular, excessive vertical and horizontal mixing could potentially disrupt DSW's properties as it flows down the continental slope. Heuzé et al. (2013) suggested that modeled DSW in most coarse-resolution models mixes with intermediate waters before it can reach the bottom of the continental slope.

Mid- to high-resolution models (horizontal resolution about 0.1–0.25°) yield more realistic AABW production (Kiss et al., 2020; Newsom et al., 2016; Snow et al., 2016). They can also reproduce the export of DSW from the shelf to the oceanic basins, but with significant underestimation of the dense water volume transport and its variability (e.g., Kerr et al., 2012; Kusahara et al., 2017; Sasai et al., 2004). In these cases, either the quality of the bathymetric dataset (Kerr et al., 2012) or the horizontal resolution of the model (10–20 km, Kusahara et al., 2017) were insufficient to resolve the canyons and troughs through which the DSW flows. Resolving topographic corrugations of order (10^0 km) is indeed crucial to properly reproduce dense water outflows through a continental slope (Matsumura and Hasumi, 2010, 2011; Muench et al., 2009a). Some studies using models with horizontal resolutions ranging from 2 to 10 km on the Antarctic shelf and slope regions (e.g., Kusahara et al., 2010; Morrison et al., 2020) show seemingly realistic DSW pathways, but do not provide a systematic comparison with observed pathways or AABW properties. Kusahara et al. (2010, 2017) also noted that the vertical and horizontal resolutions of their model may still be insufficient to properly model AABW formation. This is likely due to spurious vertical mixing generated by step-like bottom topographical changes for horizontal resolutions of order (10^1 km) and vertical resolutions of order (10^1 m) (Wang et al., 2008). More generally, the vertical and horizontal resolutions needed in a model to reproduce dense water plumes depend on the plume thickness and the continental slope steepness (Winton et al., 1998).

Here we sought to simulate the formation and descent of DSW off Cape Darnley and investigate its sensitivities to horizontal and vertical grid spacings. This study focused on the Cape Darnley Polynya (CDP) region in East Antarctica, as this is one of the main regions of AABW formation (Ohshima et al., 2013). There have been several studies of this region, including oceanographic observations, remote sensing, and numerical modeling (Aoki et al., 2020; Fraser et al., 2019; Hirano et al., 2015; Nakayama et al., 2014; Nihashi and Ohshima, 2015; Ohshima et al., 2013; Tamura et al., 2016; Williams et al., 2016; Wong and Riser, 2011). Nakayama et al. (2014) studied the CDP region using a model with realistic settings and forced with a constant surface salt flux between March and October to simulate the effects of sea ice production. With this configuration, the model was able to reproduce DSW formation and its downslope flow in the region. That study also elucidated the dynamics responsible for the periodic outflow of DSW previously observed by Ohshima et al. (2013).

The present study builds up on Nakayama et al.'s (2014) work by developing a coupled ice-ocean model in the CDP region with realistic wind forcing and improved bathymetry data. The model setting and its validation are described in Section 2 and Section 3, respectively. We conducted sensitivity experiments to study the importance of fine-scale bathymetry, which may be required to accurately represent the

Table 1

Model parameters used for the simulations in this study. Only those parameters that differ from Nakayama et al.'s (2018) model configuration are indicated in the table.

Parameter	Value
Air/sea ice drag coefficient	$2.5 \cdot 10^{-3}$
Lead closing (m)	0.5
Sea ice dry albedo	0.83
Sea ice wet albedo	0.77
Snow dry albedo	0.89
Snow wet albedo	0.77

formation and descent of DSW (Section 4). We then discussed the implications of our results on the modeling of AABW formation in other regions (Section 5). We also compared our model output with the results from the Estimating the Circulation and Climate of the Ocean (ECCO) state estimate (ECCO Consortium et al., 2019, 2021; Zhang et al., 2018), the solution of a global, free running, coupled, ice-ocean model, which served as a base configuration to our model (Section 3).

2. Model and experimental setup

The model was an eddy-resolving, regional configuration of the MITgcm (Marshall et al., 1997) for the CDP region with hydrostatic approximation and dynamic/thermodynamic sea ice (Losch et al., 2010). Our configuration was similar to that of Nakayama et al. (2018) with some adjustments to the model parameters that are indicated in Table 1. Nakayama et al.'s (2014) model in the CDP region used constant surface salt flux to represent the effects of sea ice formation. Good representation of ocean-ice processes should benefit the modeling of dense waters (Kerr et al., 2009; Renner et al., 2009), and as such, the main improvement we brought to Nakayama et al.'s (2014) configuration was the inclusion of sea-ice modeling. Our model also included realistic wind forcing, and we improved the quality of the bathymetric dataset by including newer, high-resolution bathymetry data in the vicinity of the Wild Canyon (Fig. 1), the most crucial area within the model domain. The model simulation was conducted for the year 2008, and the model was forced using the European Centre for Medium-Range Weather Forecast (ECMWF) 6-hourly atmospheric data from the ERA-Interim reanalysis product. We applied a permanent fast-ice mask based on Fraser et al. (2019, 2020); Fig. 1, green shading). The horizontal coordinate system was cartesian, and the vertical coordinate system was a z-grid with shaved grid cells (Adcroft et al., 1997). We conducted a 1-year spin-up of the model at a horizontal resolution of 4-km and with a 50-layer vertical grid (see next chapter). The spin-up was initialized from a historical conductivity, temperature, and depth (CTD) dataset (Boyer et al., 2018; Treasure et al., 2017, see Section 3.1) mapped following Shimada et al. (2017). We then used the spin-up temperature and salinity output on day 366 as initial conditions for all the sensitivity experiments (Table 2). A test simulation at 4-km resolution was conducted, initialized with a 2-year spin up, and yielded similar results as the simulation with a 1-year spin-up. The current velocity was uniformly set to 0 m s^{-1} as the initial condition. The temperature and salinity boundary conditions were obtained from seasonal climatologies estimated from our historical CTD dataset following Shimada et al. (2017). The ocean current and sea ice boundary conditions were obtained from the monthly ECCO LL270 state estimate (Zhang et al., 2018). A passive tracer was restored to unity at the surface with a restoring time scale of an hour to detect the main pathways of DSW across the slope.

We designed various experiments using different horizontal and vertical resolutions (Table 2). The finest horizontal resolution was 1 km, and the coarsest resolution was 16 km, close to that of the ECCO product. The 16 km case may then represent the production and descent of DSW in coarse-resolution global circulation models. We also ran a 40-m vertical, 2-km horizontal resolution (40m2km) experiment with a 16-km resolution bathymetry linearly interpolated to the 2-km

Table 2

Summary of the different experimental cases of the model.

Horizontal resolution	16 km	8 km	4 km	2 km	2 km 16 km-interpolated bathymetry	1 km
Vertical resolution						
ECCO	ECCO16km ^a	ECCO8km	ECCO4km	ECCO2km	–	ECCO1km
40-m	40m16km	40m8km	40m4km	40m2km	40m2kmS	40m1km
20-m	20m16km	20m8km	20m4km	20m2km	–	20m1km
10-m	10m16km	10m8km	10m4km	10m2km	–	–

^aECCO16km: Vertical resolution is the ECCO grid resolution; horizontal resolution is 16 km. Similarly, 40m2km indicates a vertical resolution of 40 m and a horizontal resolution of 2 km.

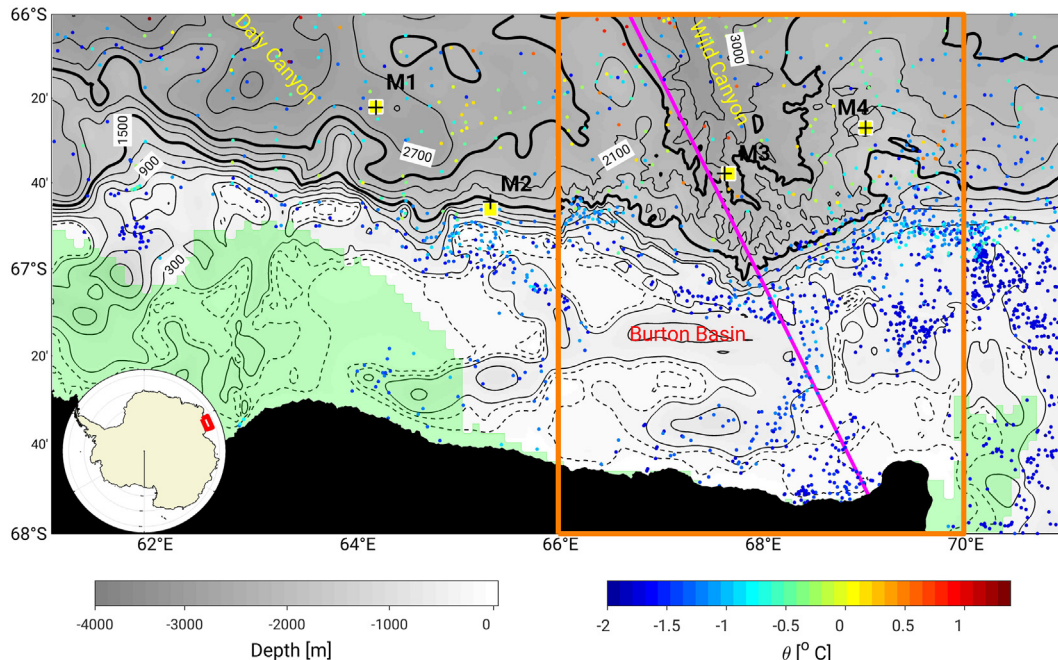


Fig. 1. Bathymetric map of the model domain (gray shades) and available historical data at 200 m depth (colored dots). The green shade represents the land-fast ice mask used in our model and determined following the method described in Fraser et al. (2019). The solid Magenta line represents the cross section along which data are plotted in Figs. 2 and 3. The four moorings of Ohshima et al. (2013) used for comparison in this study are plotted as yellow squares, and the black crosses represent the locations of the moorings in the model, which were slightly offset in order for the bottom depth of the model to match the bottom pressure recorded at the moorings location. Thin solid black lines represent isobaths plotted at every 300 m, and the thick solid black lines represent the 1500-m and 2400-m isobaths. The 100-m and 200-m isobaths are plotted as thin dashed black lines. The area within the orange box includes bathymetric data recently acquired by R/V *Hakuho-maru* and *Shirase*. The area within the red box in the inset represent the model domain.

resolution grid (this experiment is hereafter referred to as the “2-km smoothed case”) to assess how the accuracy of the bathymetric data may affect the downslope flow of DSW. The coarsest vertical resolution was that of the ECCO product, whose 50 layers varied from a width of 10-m at the surface to 465-m at a depth of 5000 m. The 40-m vertical grid had the same resolution as the ECCO grid for those cells whose width was smaller than 40 m, and all other grid cells had a width of 40 m. The 20-m grid was built following the same principle, and all cell widths for the 10-m grid were 10 m.

3. Data and validation

3.1. Datasets

3.1.1. Bathymetry data

The model bathymetry data were based on ship-based multibeam echo sounder data and the global relief model ETOPO1 (Amante and Eakins, 2009). Multibeam bathymetric data were acquired by a 20-kHz frequency SeaBeam3020 system (L3 Communications ELAC Nautik) installed on the R/V *Hakuho-maru* and Japanese icebreaker *Shirase*. The data were acquired during three *Hakuho-maru* cruises in February–March 2008 (cruise KH-08- leg 4), January–March 2016 (cruise KH-16-leg 1), and January–February 2019 (cruise KH-19- leg 1) and five successive Japanese Antarctic Research Expeditions (JARE) from 2009

to 2013 (JARE No. 51–55). The *Shirase* data were provided by the Japanese Coast Guard for scientific utilization. Most of the multibeam bathymetric data were acquired in the vicinity of the Wild Canyon on the eastern half of the domain and cover about 60% of the area within the orange box in Fig. 1.

The sound velocity was corrected with real-time data of the surface water velocity, deep-sea observations of CTD cast, and expendable CTD (XCTD) profiles. The CARIS HIPS and SIPS software (Teledyne CARIS Inc., Ltd., Fredericton, Canada) was used for raw data processing. The remaining blanks in the bathymetric map were interpolated using the global relief model ETOPO1 at 1 arc-minute intervals. The bathymetric model with a 500-m resolution was finally generated using all data mentioned above. Data were processed using the GMT system (Wessel et al., 2013), and the bathymetric data were gridded using a weighted nearest-neighbor algorithm and surface algorithm using adjustable tension continuous curvature splines.

3.1.2. Hydrographic and current velocity data

Historical temperature and salinity data acquired in the CDP region were used to validate the model results. The dataset mostly comprised biologging data from the Marine Mammals Exploring the Oceans Pole to Pole consortium (Treasure et al., 2017), which constitutes the largest source of CTD data in the polar regions. Most of the data on the continental shelf (Fig. 1) were acquired via biologging. This dataset was

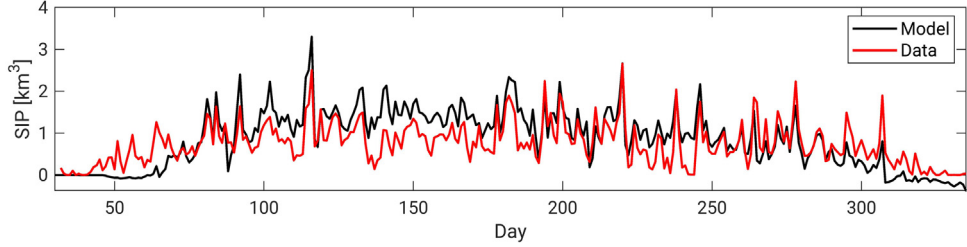


Fig. 2. Time series of daily-integrated sea ice production (SIP) in the CDP region for the year 2008, estimated from (red) AMSR-E data following Nakata et al. (2021) and (black) the model control run.

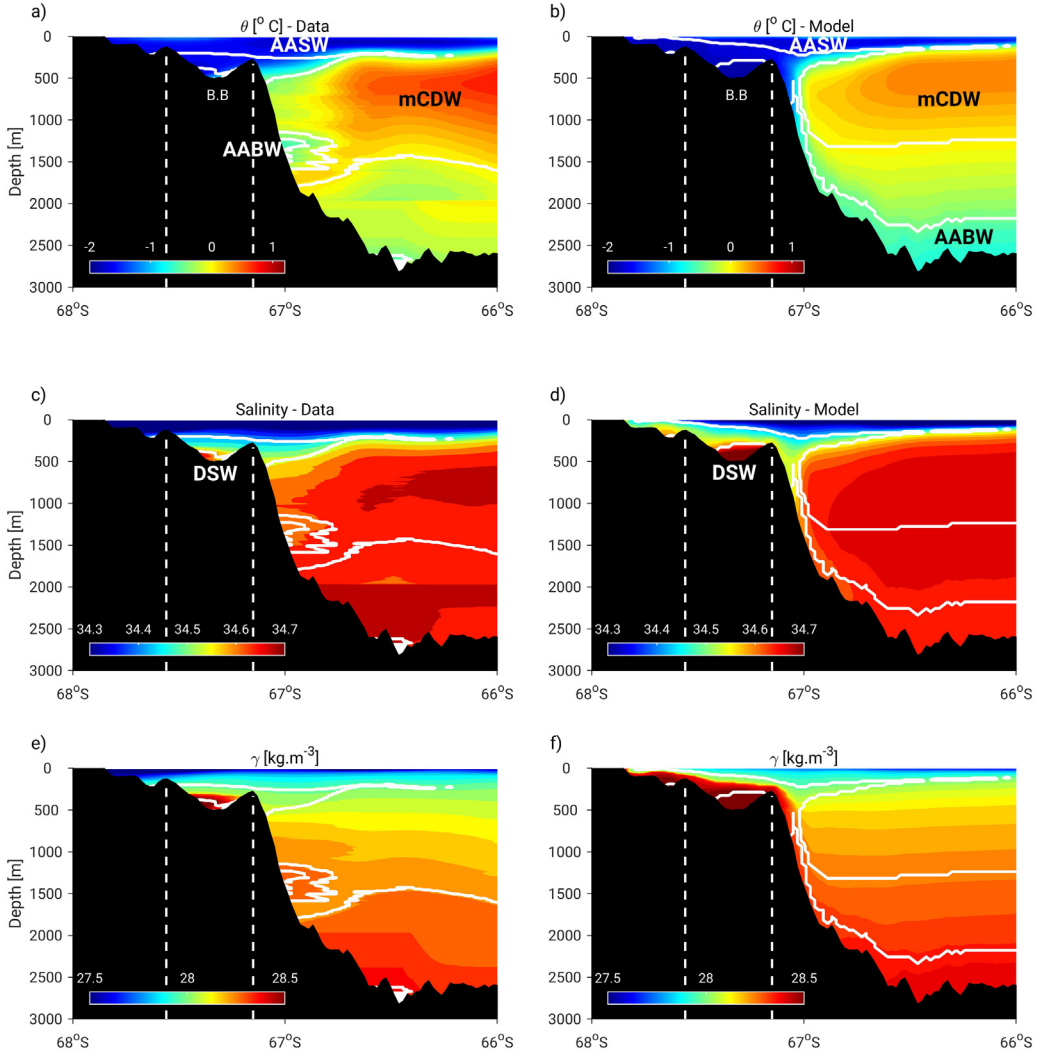


Fig. 3. Cross section of potential temperature data averaged from (a) all historical data points, and (b) model control run for the year 2008. (c, d), and (e, f) respectively represent the cross sections of salinity and neutral density for the observation and model data. Observation data here refers to data acquired from both instrumented seals (biologging), historical CTD and Argo floats, weighted-averaged within 50-km wide bins along the section. Weights were established from a Gaussian distribution with an e-folding scale of 25-km, arbitrarily chosen to conserve details in the horizontal structures of the water column. The white dashed lines represent the limits of the Burton Basin, noted "B.B" in panels (a) and (b). Water masses defined in Section 3.2.1 are indicated in panels (a-b) and (c-d).

supplemented by Argo floats and historical CTD data obtained from the World Ocean Database 2018 (Boyer et al., 2018). A total of 1934 data points exist within the model domain at a depth of 200 m. Data were mostly acquired between 2007 and 2017.

The M3 mooring was located in the Wild Canyon (Fig. 1) and deployed at a depth of 2608 m, recording temperature, salinity, and current velocity at discrete depths from ~26–224 m above the bottom. The M3 data constitute the main comparison data here because Ohshima et al. (2013) primarily observed DSW descent at this location.

To compare the velocity between the model and observation, a time series based on data ~220 m above the bottom was used because the meridional velocity at M3 in the model was not defined in the bottom-most cell at most resolutions. The M3 velocity time series at 224 and 26 m above the bottom had comparable characteristics. The current at M3 is bottom intensified (Ohshima et al., 2013), and the main difference between the current velocity at the two depths is a smaller amplitude of variations at 224 m (~0.3 m s⁻¹) than at 26 m above the bottom (~0.5 m s⁻¹). The comparison for the temperature and salinity was based

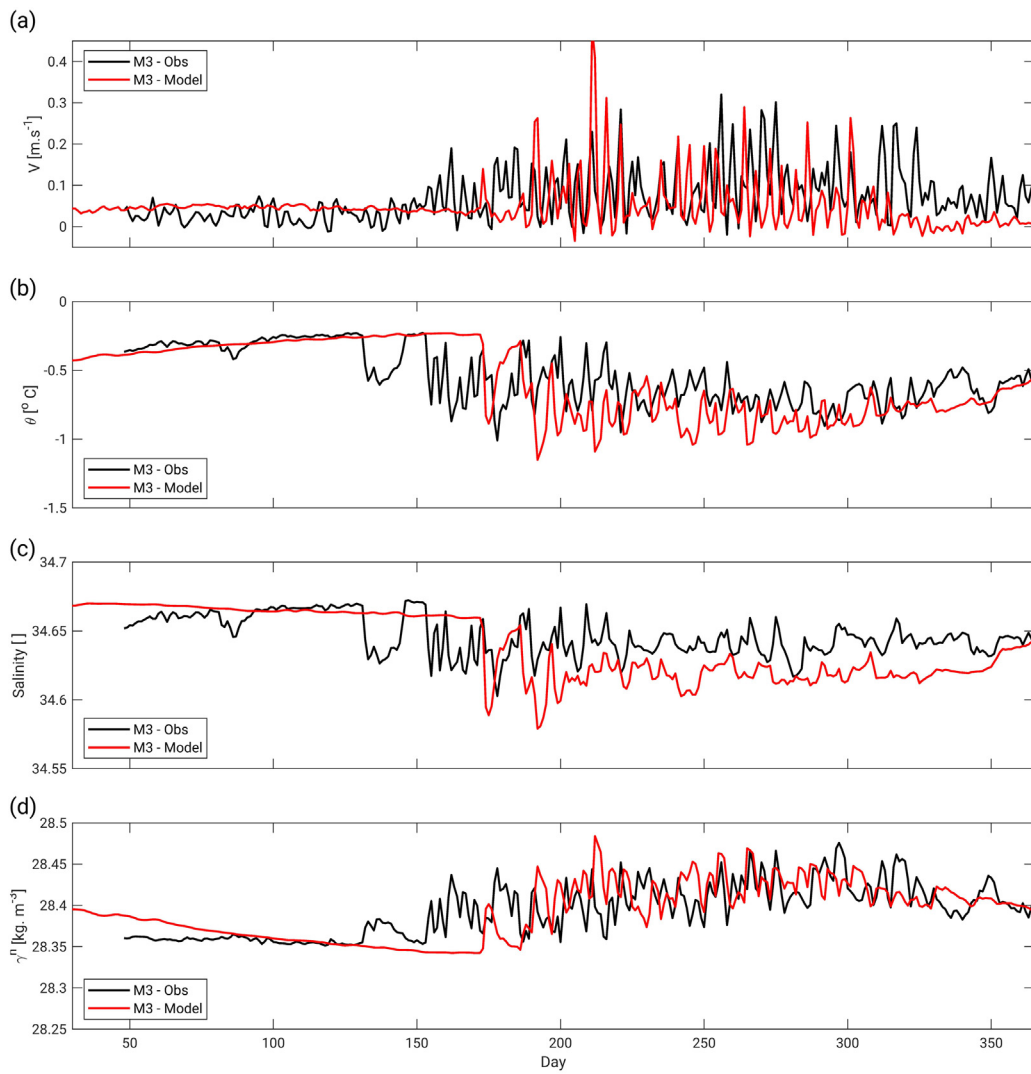


Fig. 4. Comparison of observation and model control run (40m2km) data at the M3 mooring in 2008. (a) Near-bottom velocity along the current main axis, for the observation (224 m above bottom) and the model (240 m above bottom). (b) Bottom potential temperature, (c) salinity, and (d) neutral density.

on data located 20 m above the bottom. We refer to the data 200 m above the bottom as near-bottom and the data 20 m above the bottom as bottom data. A comparison of the model data with time series at M1, M2, and M4 (Fig. 1) was conducted as well (Section 4.2).

3.1.3. Water masses definition

The main water masses discussed in our study are DSW and AABW. We defined these two water masses in the θ -S space based on Ohshima et al. (2013). Specifically, AABW is the water with neutral density $\gamma \geq 28.27 \text{ kg m}^{-3}$ and potential density $\theta < -0.4^\circ\text{C}$, and DSW is the water with $\theta \leq -1.26^\circ\text{C}$ and $S \geq 31.61$. Other water masses mentioned in this paper were defined according to Orsi and Wiederwohl (2009), namely Antarctic Surface Water (AASW) with $\gamma < 28.00 \text{ kg m}^{-3}$, and mCDW with $28.00 < \gamma < 28.27 \text{ kg m}^{-3}$.

Because AABW exists permanently at the bottom of the continental slope in the CDP region (Aoki et al., 2020), the production of newly formed AABW was estimated by calculating the volume of water below 2000 m depth, colder than -0.4°C and with a tracer concentration greater than 0.05 (Section 4.1). When analyzing the tracer experiment results (Figs. 6–8), we may use the more generic term “dense water” when referring, regardless of its depth, to water colder than -0.4°C and with a tracer concentration greater than 0.05.

3.2. Model evaluation

3.2.1. Sea ice production

We first evaluated the model sea ice production of the 40m2km experiment (control run) against sea ice production estimated from Advanced Microwave Scanning Radiometer-Earth Observing System (AMSR-E) data following Nakata et al. (2019, 2021). The time series of daily observed and modeled sea ice production (Fig. 2) were in good agreement ($R = 0.76$) for most of 2008. The seasonal pattern in the model and (satellite) observations were consistent, and remarkably, the short-term variability in the model also agreed well with that of the observations, e.g., between day 193–205 and day 262–276. The modeled sea ice production was only slightly larger on average ($0.87 \text{ km}^3 \text{ day}^{-1}$) than the observations ($0.75 \text{ km}^3 \text{ day}^{-1}$), and lasted for a shorter duration (day 65–308 vs. day 25–320). Such discrepancy between model and data can be considered small, though.

3.2.2. Time-averaged hydrography

The results of the control run were compared to historical data along a cross-section through Wild Canyon (Fig. 1). The data within this cross-section were averaged over the year 2008 for the model and all available years for the observations. The model and observations showed the same vertical distribution of water masses towards the offshore and the influence of DSW on the shelf. Specifically, for

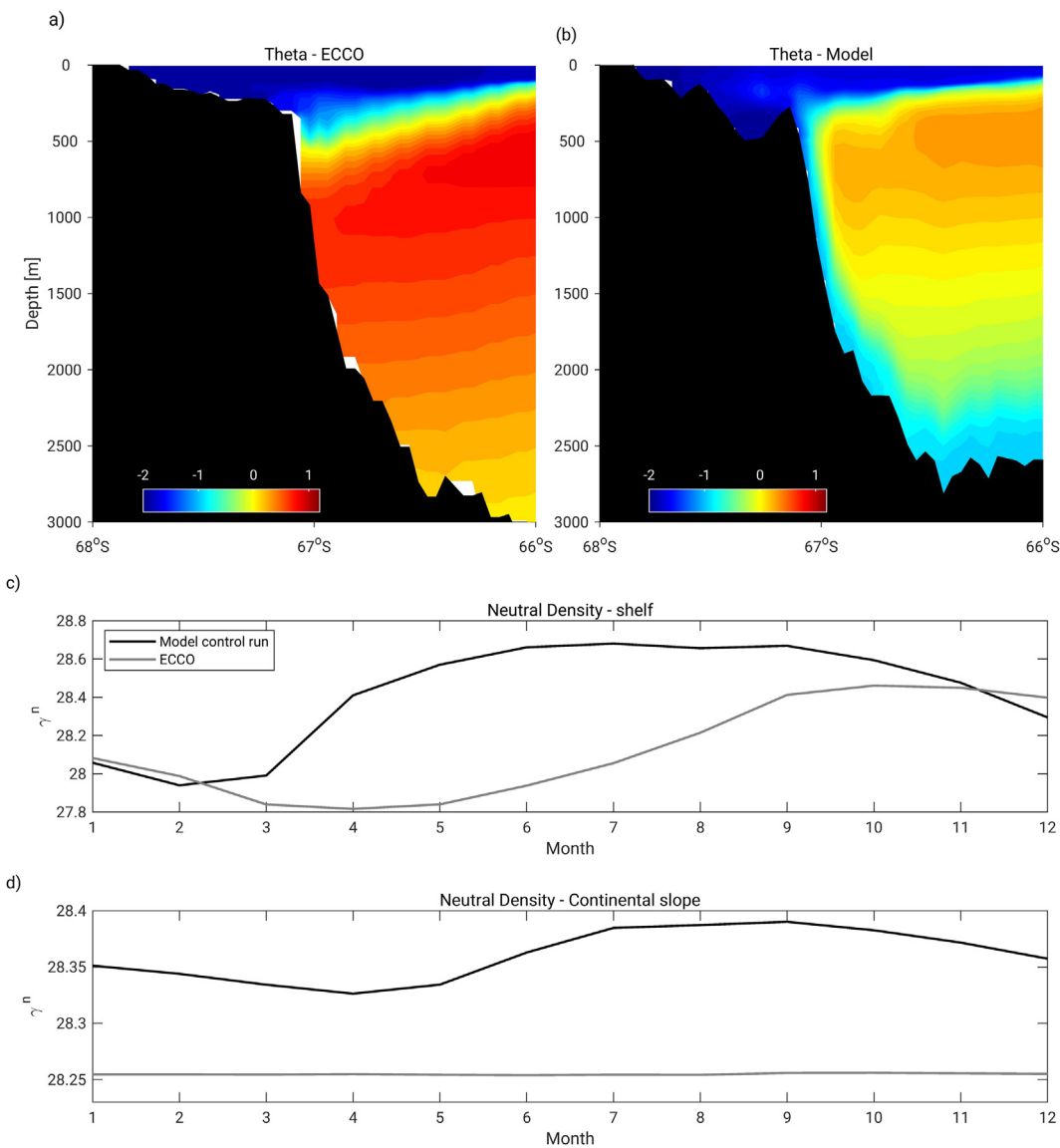


Fig. 5. Cross section of temperature data for September 2008 from (a) the ECCO state estimate and (b) the model control run. (c) Monthly time series of neutral density at 100 m spatially averaged over the shelf regions in the model domain for the year 2008 for the ECCO state estimate (solid gray line) and the model control run (solid black line). (d) Monthly time series of neutral density at 1900 m averaged over the continental slope regions within the model domain.

both model and observations, the water column on the offshore side exhibited a ~100–200-m thick layer of cold ($\theta < -1^\circ\text{C}$, Fig. 3a–b) and fresh ($S < 34.4$, Fig. 3c–d) Antarctic Surface Water above the warmer ($0^\circ\text{C} < \theta < 1^\circ\text{C}$) and saltier ($S > 34.6$) mCDW. Besides, DSW was present on the shelf at the bottom of the Burton Basin in both sections (noted B.B in Fig. 3a–b). This DSW was likely produced in winter and subsequently stored in the basin (Nakayama et al., 2014); it had the highest neutral density ($\gamma^n \geq 28.5 \text{ kg m}^{-3}$) of the entire section, a typical property of the DSW formed in the CDP region (Williams et al., 2016). AABW was present in the model along the slope down from 800 m depth and covered the oceanic basin up to 500 m above the bottom (Fig. 3b, d, f). Few observations were available below 2000 m (note the discontinuity in values at 2000 m in Fig. 3a, c) and traces of AABW were only present along the slope around 1300 m depth in the observation section (Fig. 3a, c, e).

The model data on the shelf poleward of the Burton Basin was colder by ~0.2 °C and saltier by ~0.3 than observations. This is likely because of the very small number of observations in winter (when the water on the shelf is colder and saltier). The root mean square

(RMS) difference in temperature and salinity between the simulated and observed sections for the respective ranges of 0–200 m and 200–2000 m were 0.27 and 0.09 for salinity, 0.33 °C and 0.38 °C for temperature, and 0.36 kg m⁻³ and 0.28 kg m⁻³ for neutral density. These differences between the model and observations may be due to (1) the scarce distribution of observations, with data averaged within a 50-km radius of each point along the section; and (2) the low number of observations in winter resulting in an underrepresentation of periods of DSW formation and downslope flow in the dataset. Because the observations are averaged over more than 10 years (with data mainly acquired between 2007 and 2017), interannual variabilities could also be responsible for some of the discrepancies.

3.2.3. Time series at bottom mooring M3

The modeled time series of the near-bottom and bottom properties at M3 showed notable similarities with the time series obtained from the mooring data. The observed flow 224 m above the bottom at M3 was characterized by a very weak and steady current until day 152 (Fig. 4a). After this day, high-frequency variations with ~5-day

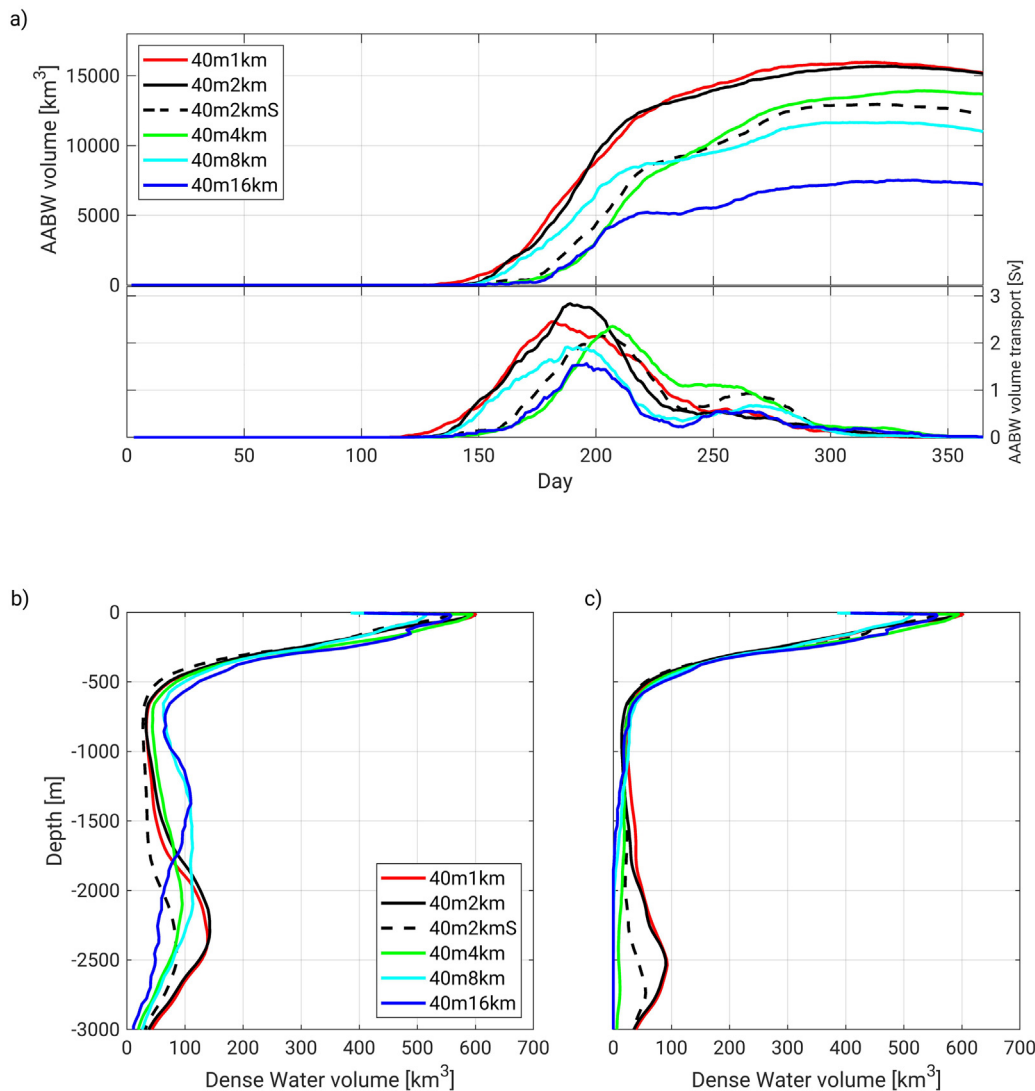


Fig. 6. (a) Time series of (top) AABW volume below the depth of 2000 m and (bottom) AABW volume transport through the 2000 m depth in the model for all horizontal resolutions at a fixed 40-m vertical resolution. (b) Profiles of dense water volume per 10-m thick layers averaged between day 180 and day 270 for the same series of experiments. In (a), AABW refers to water with potential temperature $< -0.4^{\circ}\text{C}$ and tracer concentration > 0.05 below 2000 m. In (b), dense water refers to water with potential temperature $< -0.4^{\circ}\text{C}$ and tracer concentration > 0.05 , regardless of its depth, i.e. near-surface dense water is DSW, and near bottom dense water is AABW. (c) same as (b) but where the criterion for potential temperature is set to $< -0.7^{\circ}\text{C}$.

period (Oshima et al., 2013) and with a maximum amplitude of $\sim 0.3 \text{ m s}^{-1}$ occurred until around day 330. High-frequency oscillations still occurred after day 330, albeit with a smaller amplitude. The time series of the modeled current velocity showed high-frequency oscillations (Fig. 4a), but only between day 172 and day 315. The shorter time span of modeled vs. data high-frequency oscillations could be related to the shorter duration of the sea ice production season in the model (Fig. 2).

In the observed temperature and salinity time series, a sudden drop by about 0.5°C occurred around day 150, as the current velocity started to oscillate (Fig. 4b, c). This drop was followed by high-frequency variability similar to that of the current. The modeled temperature and salinity abruptly dropped similarly to the observations and showed a comparable high-frequency variability, lasting only between day 172 and day 315 as well. Besides, modeled temperature and salinity during this period were lower than the observations, respectively by 0.13°C and 0.02 on average. These negative biases are reasonable when compared to other high-resolution models in the Southern Ocean (e.g., Newsom et al., 2016; Nakayama et al., 2018) and compensated each other in terms of neutral density, resulting in

an insignificant averaged difference (0.00 kg.m^{-3}) in γ^n between model and data.

3.3. Evaluation of the ECCO state estimate in the CDP region

We present the simulated hydrography in the Cape Darnley region of a well-known global ice-ocean model (ECCO LLC270 Zhang et al., 2018) also based on MITgcm. We note that many other global and regional simulations (e.g., the Southern Ocean State Estimate (SOSE, Mazloff et al., 2010), or the Simple Ocean Data Assimilation (SODA, Carton and Giese, 2008)) are capable of simulating AABW production better than ECCO LL270 and we show the simulated results of the ECCO LL270 state estimate as an example because our surface boundary conditions and lateral boundary conditions of ocean current came from this state estimate. The reader is referred to Azaneu et al. (2014) and Dotto et al. (2014) respectively, for a full assessment of a previous version of ECCO, and a comparative study of reanalysis products in the Weddell Sea.

The output from the model's control run and ECCO for September 2008 were compared along the same cross-section as in Fig. 3. Evidence

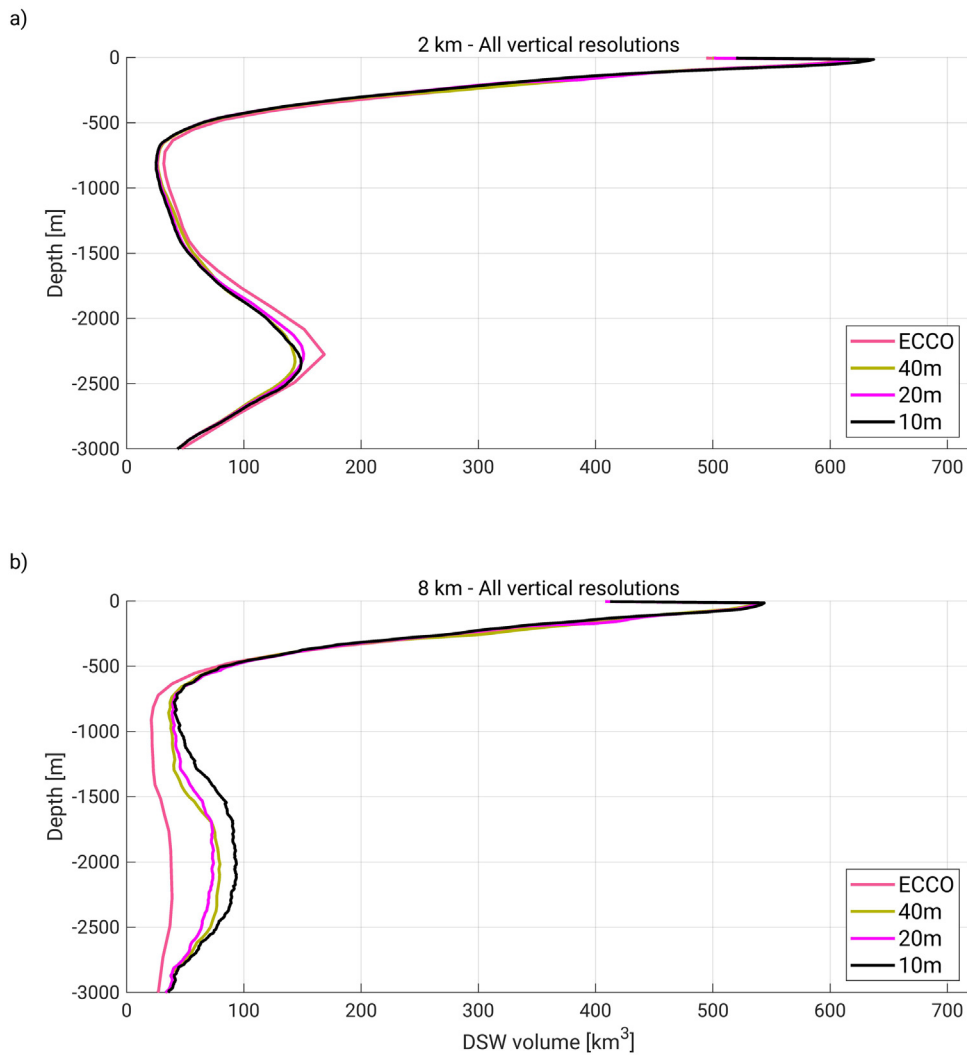


Fig. 7. Profiles of DSW volume per 10-m thick layers averaged between days 180–270, estimated for (a) all vertical resolutions at a fixed 2-km horizontal resolution and (b) all vertical resolutions at a fixed 8-km horizontal resolution.

of DSW production in both models is suggested by the presence of very cold water ($\theta < -1.5^{\circ}\text{C}$) on the shelf (Fig. 5a–5b) with temperature close to the freezing point, consistent with observed DSW properties (Aoki et al., 2020; Ohshima et al., 2013; Williams et al., 2016). The production of DSW in ECCO and our model is also evident in the monthly time series of neutral density in 2008 averaged over the shelf regions at a depth of 95 m (Fig. 5c). Both time series indeed showed a strong increase ($\sim 0.6\text{--}0.7 \text{ kg.m}^{-3}$) in neutral density starting in March (model) or May (ECCO), with the maximum density reached in September (model) or October (ECCO). The delay in density increase in ECCO was likely caused by an approximately 80% underestimation of the polynya area – within the model's domain – in the state estimate (not shown). The underestimate of the polynya area in ECCO may be related to the choice of air-drag coefficient.

Along and near the bottom of the continental slope, the differences between the model and ECCO data suggest that the DSW produced near the surface by ECCO did not flow down the slope. In our model, DSW downslope flow was evident from the cold waters ($\sim -1^{\circ}\text{C}$) present all along the continental slope, from the shelf break at around 400 m to the bottom of the oceanic basin at around 2500 m (Fig. 5b). In contrast, waters colder than 0°C did not exist beyond 500 m in the ECCO state estimate section (Fig. 5a). Large differences also existed between the two models' output in the time series of neutral density averaged over the slope regions at a 1900 m depth (Fig. 5d). In our model, the neutral

density started to increase in May, two months after the onset of DSW and sea ice production, consistent with Ohshima et al.'s (2013) observations at M3. In ECCO, the neutral density time series did not show any time variation, indicating that no dense water reached this depth. Such a problem was also documented in the Weddell Sea for ECCO2 by Azaneu et al. (2014), who suggested that both changes in resolution and parametrisation (e.g. vertical mixing, convective processes) could help to improve the modeling of AABW in ECCO.

4. Results

4.1. Sensitivity on horizontal and vertical resolutions

4.1.1. AABW volume

The dense water volumes obtained from different horizontal resolutions (at a fixed vertical resolution of 40 m) suggest that resolutions of 2 km or better can produce AABW in reasonable amounts that reaches the bottom of the continental slope (Fig. 6) (AABW refers to waters with potential temperature less than -0.4°C and tracer concentration greater than 0.05). Although experiments at all resolutions yielded a significant volume of AABW below 2000 m, the maximum AABW volume was strongly dependent on resolution, increasing from 7100 km^3 (16-km) to $15,900 \text{ km}^3$ (1-km). The time series of the 2-km

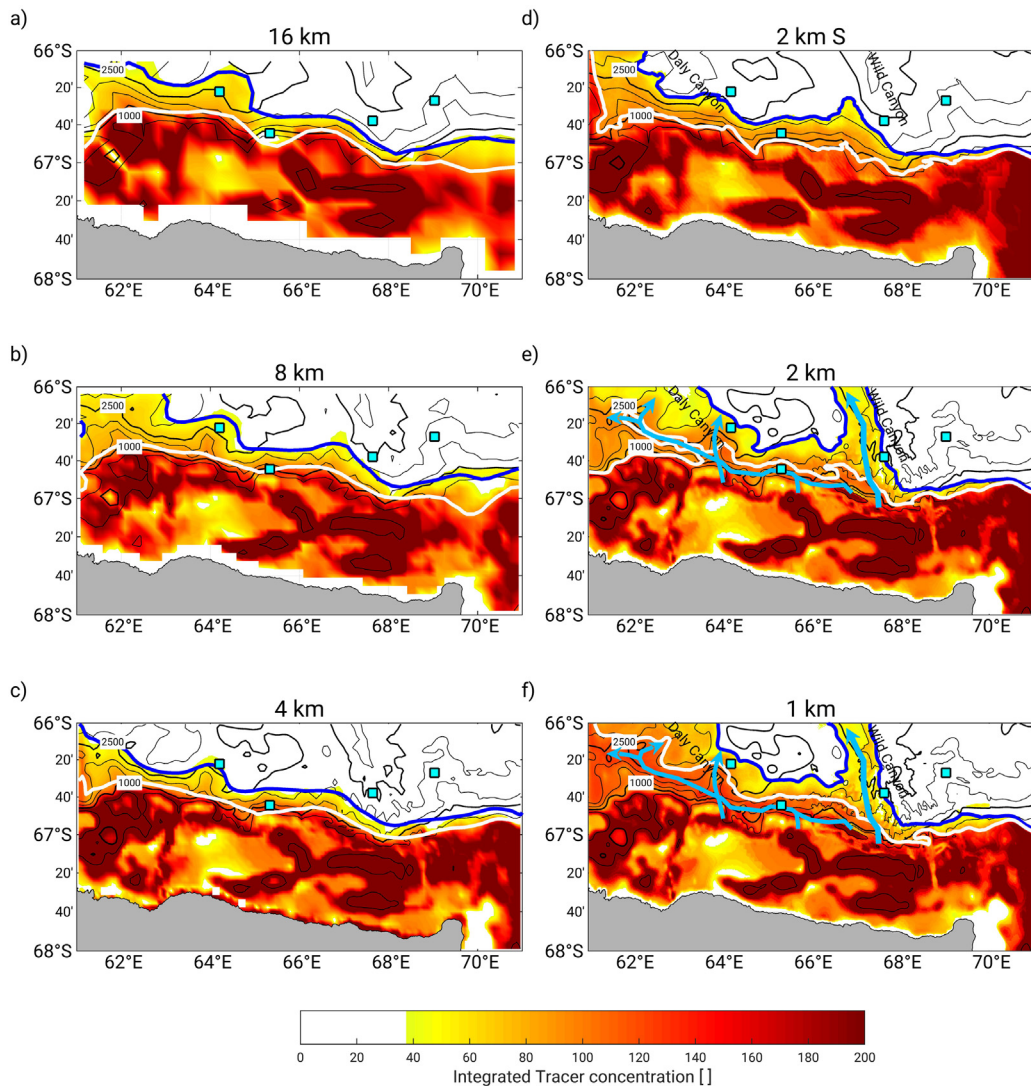


Fig. 8. Vertically integrated tracer concentration averaged between day 170–day 220 for the 40-m vertical resolution experiments at horizontal resolutions of (a) 16-km, (b) 8-km, (c) 4-km, (d) 2-km smoother bathymetry, (e) 2-km, and (f) 1-km. The four squares represent the position of each mooring in the model. The isobaths are plotted every 500 m as thin solid black lines and the thick solid black lines represent the 1000 m and 2500 m isobaths. The thick solid white and blue lines represent the contour of 100 (Iso100) and 40 (Iso40) tracer concentration, respectively. The tracer concentration was vertically integrated within 400 m of the bottom. Pathways are represented by light blue arrows in (e) and (f).

and 1-km cases were comparable, which suggests a 2-km resolution threshold.

We estimated the daily volume transport by calculating the time derivative of the daily volumes (Fig. 6a). The annual volume transports for the 1-km and 2-km resolution cases (0.51 Sv and 0.50 Sv, respectively) were consistent with previous estimates of ~0.5 Sv of AABW transport in the Wild Canyon (Ohshima et al., 2013; Nakayama et al., 2014). The 4-km and 8-km resolution experiments also yielded reasonable yearly-averaged estimates (0.44 Sv and 0.38 Sv, respectively), despite large differences in the time series compared with the 1-km or 2-km cases (Fig. 6a). Only the 16-km resolution case annual volume transport (0.26 Sv) was inconsistent with previous estimates.

The depth–volume profiles averaged between day 180 and day 270 (Fig. 6b) suggest that for resolutions of 8-km and less, large amounts of dense water stayed mid-depths, whereas for resolutions of 2-km and more, most dense waters flowed towards the slope's bottom. For example, the largest volume of dense water below 500 m was found at 1300 m depth (~110 km³) for the 16-km resolution, and at 2350 m for the 1-km and 2-km resolutions (140 km³). Changing the

criterion of AABW definition to $\theta < -0.7^{\circ}\text{C}$ instead of $\theta < -0.4^{\circ}\text{C}$ resulted in little to no AABW below 2000 m for resolutions lower than 4-km, but still significant AABW amounts (95 km³ at 2350 m) for the 1-km and 2-km resolution cases (Fig. 6c). This suggests that at low ($\leq 4\text{-km}$) resolutions, even though some dense water flowed down to below 2000 m depth (Fig. 6a–b), DSW warmed excessively along its way to the bottom. We suggest – as Heuzé et al. (2013) did – that a large portion of DSW was changed into intermediate water, thus explaining why the maximum volume of dense water was found at mid-depth (Fig. 6b). The warming and concurrent loss of density of the dense water were possibly due to excessive convective mixing with surrounding waters (Winton et al., 1998).

Reducing the quality of the bathymetric dataset significantly decreased the production of AABW. The volume time series of the 2-km smoothed case were similar to those at 4 km resolution (Fig. 6a), with a maximum AABW volume (12,800 km³) about 20% less than that of the standard 2-km resolution (15,900 km³). Meanwhile, the maximum volume in the smoothed bathymetry case (80 km³) was about half that of the standard case in the depth–volume profile (140 km³, Fig. 6b).

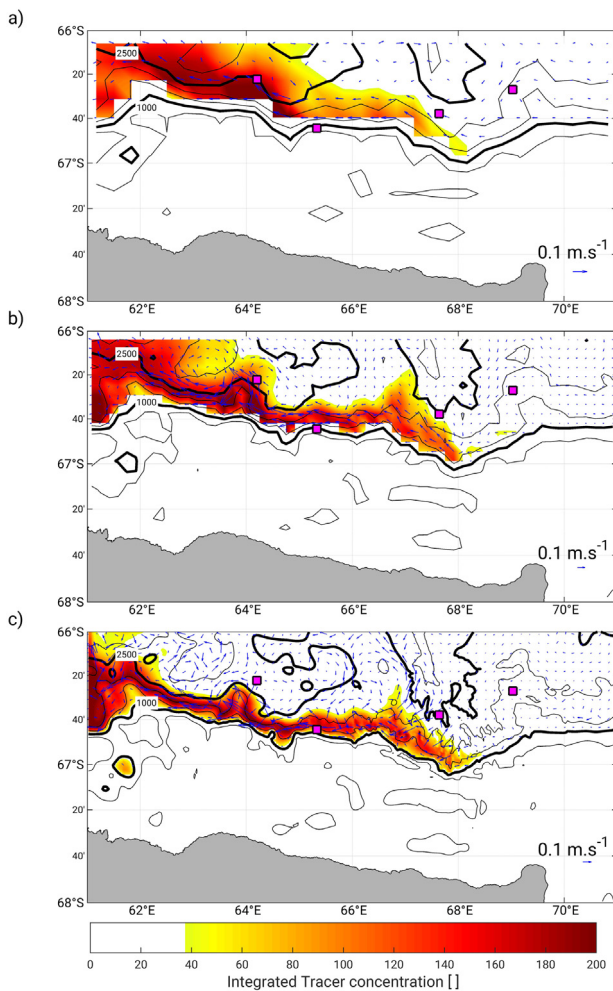


Fig. 9. Tracer concentration vertically integrated from 1000 to 2000 m depth and averaged between day 170 and 220 for the 40-m vertical resolution experiments at horizontal resolutions of (a) 16-km, (b) 8-km, (c) 2-km. The four squares represent the position of each mooring in the model. The isobaths are plotted every 500 m as thin solid black lines and the thick solid black lines represent the 1000 m and 2500 m isobaths.

Changing the vertical resolution had little influence on the volume of dense water produced and flowing to the bottom. The dense water volume profiles for all four different vertical resolutions at 2-km (Fig. 7a), 4-km, and 1-km (not shown) horizontal resolutions showed no significant difference. A slight dependence on vertical resolution existed for resolutions of 8 km (Fig. 7b) and 16 km (not shown). However, even a 10 m resolution (10m8km case) yielded significantly lower dense water volume than the 40m2km or 40m1km cases (Fig. 7b).

4.1.2. Pathways

Ohshima et al. (2013) and Nakayama et al. (2014) suggested that the downslope flow of DSW in the CDP region follows topographical features, such as underwater canyons. To evaluate the descent pathways at different horizontal resolutions, we vertically integrated the amount of tracer within 400 m of the bottom and calculated the average of this quantity (referred to as bottom tracer hereafter) between day 170 and day 220 (Fig. 8).

At low resolutions (Fig. 8a–c), the bottom tracer was mostly confined to the shelf, and only small amounts of tracer existed along the slope. The isoline of 100 tracer concentration (Iso100; thick, solid white line in Fig. 8) was generally located close to the 1000 m isobath, and the contour line of Iso40 (thick, solid blue line in Fig. 8)

reached or exceeded the 2500 m isobath. The relatively high amount of bottom tracer west of 65°E at 8-km and 16-km resolutions suggests a stronger westward advection of dense water at these resolutions. Such advection is evidenced in Fig. 9a–b, which shows the temporally averaged and vertically integrated tracer concentration between 1000 m and 2000 m (mid-depth tracer). In these cases, the largest amount of mid-depth tracer was found far offshore over the oceanic basin (depth > 2500 m) on the western side of the domain. The strong mid-depth concentration further suggests that at these low resolutions, DSW was mainly transformed into intermediate waters, and subsequently advected westward.

At high resolutions (2- and 1- km, Fig. 8e–f), high concentrations of bottom tracer existed throughout the continental slope west of 68°E. Iso100 extended beyond the 2000 m isobath and Iso40 reached the 3000 m isobath west of 64°E. Meanwhile, the mid-depth tracer (Fig. 9c) was essentially confined to the continental slope between the 1000 m and the 2500 m isobaths, consistent with a downslope flow. At these resolutions, pathways (represented by arrows in Fig. 8e–f) could be distinguished through the contours of bottom tracer Iso40 or Iso100. The most obvious pathway was a northward extension along the left flank of the Wild Canyon. Again, the 2-km and 1-km resolutions yielded comparable results (Fig. 8e–f). The tracer concentration in the 2-km smoothed bathymetry case (Fig. 8d) presented more similarities with the 8-km resolution (Fig. 8b) than with the 2-km (Fig. 8e) standard case. This further indicates the strong effect of bathymetry data quality on the downslope processes in the model.

4.1.3. Slope's bottom flow characteristics

The near-bottom and bottom variability of ocean current and hydrographic properties at the mooring M3 were described in Section 3.2.3. The time series outputs at (40-m vertical resolution) 1-km and 2-km resolutions were consistent with observational data with only minor differences. The current from the two cases exhibited a high-frequency variability comparable to that of the observations, as seen from the time series (Fig. 10a vs. Fig. 10b–c) and the energy spectra (Fig. 11a vs. Fig. 11b). Compared to the 2-km resolution case, the current at the 1-km resolution had characteristics slightly closer to the observations in terms of oscillations amplitude (Fig. 10b–c) and spectral density. In particular, the two maxima of the observed spectrum at the 5-day and 3.8-day periods (Fig. 11a) were replicated only in the 1-km case (Fig. 11b). The better definition of corrugations at 1-km resolution possibly explains this more accurate spectral definition. This is consistent with Nakayama et al.'s (2014) finding that the frequency of the downslope flow in the CDP region increases with the slope steepness.

The temperature time series of the 1-km and 2-km were remarkably similar to one another (Fig. 12b–c). The only significant difference between these two time series and the observed temperatures (Fig. 12a) consisted in the later starting dates of the oscillations (~day 170 vs. day 152). The discrepancies between the simulated ocean states at these two resolutions and the observations can be considered minor, and both 1-km and 2-km resolutions reproduced the main characteristics of the flow.

The 4-km resolution case failed to replicate observations (Fig. 10d, 12d), producing smaller amplitude oscillations (0.05 m s^{-1}) and no high-frequency variability in the temperature time series. The temperature dropped only by -0.3°C on day 197, nearly 50 days after the observations. The amplitude and frequency of the current and temperature variations in the 2-km smoothed case (Magenta line in Fig. 10c, 12c) generally resembled those at 4-km resolution. The 8-km and 16-km outputs compared poorly to observations (Figs. 10e–f, 12e–f). The velocity time series exhibited weak oscillations at 8-km resolution and no variability at 16-km resolution. The temperature time series exhibited no significant variability at these resolutions, which is consistent with the absence of dense water colder than -0.7°C beyond 2000 m depth in these cases (Fig. 6c).

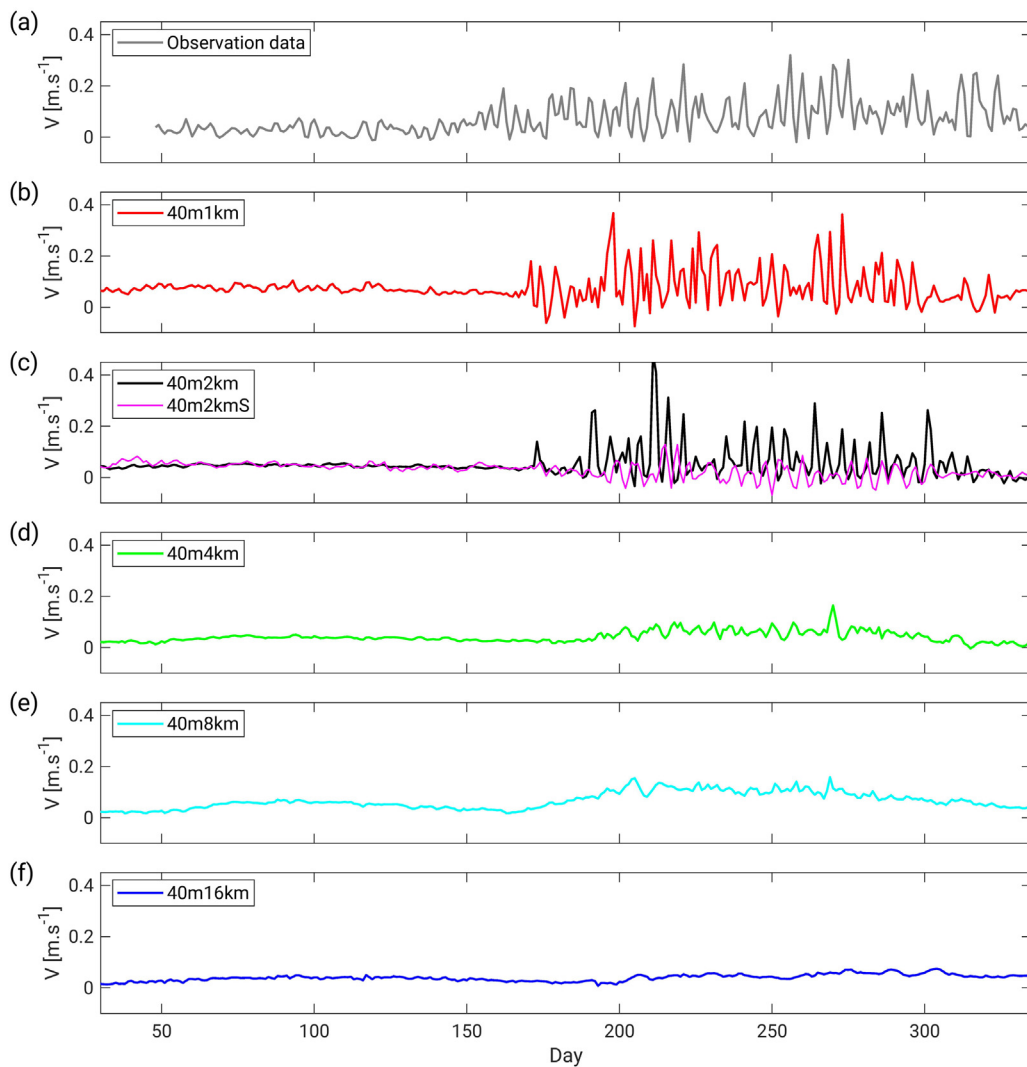


Fig. 10. Time series of meridional velocity 226 m above the bottom at the M3 mooring location from (a) observation data, and (b–f) 240 m above the bottom for the model's 40m1km, 40m2km and 40m2kmS, 40m4km, 40m8km, and 40m16km model cases, respectively.

4.1.4. AABW θ -S properties

The θ -S observations at M3 showed a sharp contrast in properties before and after day 160, with data distributed on either side of the 28.35 kg m^{-3} isopycnal (Fig. 13f). Before day 160, the θ -S properties were located along the $\sim 28.32 \text{ kg m}^{-3}$ isopycnal with little dispersion. After day 150, the water tended to become colder, fresher, and denser, and the observations were more dispersed. The AABW salinity ranged 34.60 to 34.66, the potential temperature ranged -0.5°C to -1.0°C , and the neutral density varied between 28.35 kg m^{-3} and 28.42 kg m^{-3} . The averaged properties of AABW in the CDP region (referred to as CDBW in (Ohshima et al., 2013)) are a neutral density of 28.37 kg m^{-3} , a salinity of 34.64, and a potential temperature of -0.67°C .

In the model, the changes in water properties associated with AABW formation were only observed at resolutions of 2 km or more. The increase in density, decrease in temperature and salinity, and widening of the θ -S range after \sim day 170 were seen in the 2-km (Fig. 13b) and 1-km (Fig. 13a) resolutions. The resulting averaged (between day 200 and day 300) neutral densities (respectively 28.39 kg m^{-3} and 28.37 kg m^{-3}) were very close to the observations. The model cases at the 4-km (Fig. 13d) and 2-km smoothed (Fig. 13c) resolutions produced weaker changes in temperature and salinity, leading to the averaged properties of AABW being too warm (-0.53°C) and not dense enough

(28.32 kg m^{-3}). At resolutions of 8 km (Fig. 13e) and 16 km (Fig. 13f), AABW properties were grossly underestimated, as only minor changes in temperature and salinity occurred, leading to an averaged neutral density of only 28.30 kg m^{-3} . The differences in properties for the horizontal resolutions equal to or lower than 4-km are also illustrated in the Taylor diagram (Taylor, 2001) of daily bottom neutral density at M3 (Fig. 14). A Taylor diagram summarizes in one plot the standard deviation of each time series, as well as the RMS difference and cross correlation between model and observed time series.

The results in the Taylor diagram suggest that all different vertical resolutions with a fixed horizontal resolution of 2 km yielded accurate θ -S properties, similar to those of Fig. 13b. The time series at four different vertical resolutions indeed presented nearly identical values of correlation and root mean square difference (vs. observation), and standard deviation.

4.2. Characteristics of the downslope flow at other mooring locations (1-km resolution)

In addition to M3, the model could recreate the variations of the different properties at other mooring locations, where the downslope flow presented different characteristics (Fig. 15). Ohshima et al. (2013)

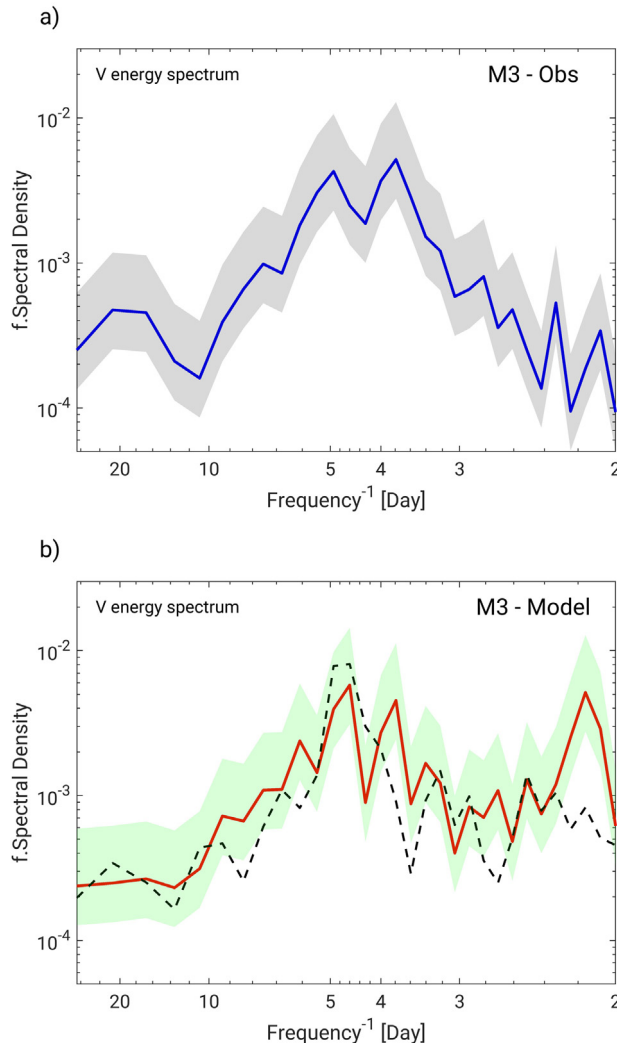


Fig. 11. Variance preserving spectra of the near bottom velocity in the main current axis at M3 for (a) observation data 224 m above bottom, and (b) the 40m1km case 240 m above the bottom. The solid lines represent the (frequency-normalized) energy spectrum and the colored shading in each panel represents the 95% confidence interval. In (b), the thin dashed black line represents the spectrum for the 40m2km case.

observed that the downslope flow of DSW at M2 occurred nearly two months before that at M3. They concluded that the earlier arrival of cold waters at M2 indicated a westward advection of the DSW at the beginning of the DSW-production season. The model captured the earlier descent of dense water at M2 (Fig. 15b) and M1 (Fig. 15a), albeit with a significant lag (25 to 30 days) to the observations. At M4, the model only reproduced the lower-frequency variability ($T > 20$ days), but not the higher-frequency signal (Fig. 15d). Williams et al. (2016) demonstrated that in the region of the M4 mooring, the water properties near the bottom are influenced by fresher modified shelf water originating from the Mackenzie Bay Polynya. The Mackenzie Bay Polynya is located southeast and outside of our model domain, and the fresher DSW produced there is transported northwards towards the CDP via the Prydz Channel. We surmise that the discrepancies between observations and model data at M4 are due to the exclusion of this upstream source of fresher dense water from our model domain.

5. Discussion

5.1. Horizontal and vertical resolutions required for the Cape Darnley region

The vertical and horizontal resolutions required for accurately modeling density-driven downslope flows depend on the plume thickness and the slope angle (Winton et al., 1998). Specifically, for a plume of layer thickness H flowing over a slope of angle α , the vertical resolution R_V must be finer than $H/2$ and the horizontal resolution R_H should satisfy $R_H \leq R_V / \alpha$. Our results demonstrated that resolutions of 2-km or higher are necessary to accurately reproduce the AABW formation process, whereas vertical resolution had little effect on the model performance. We now reexamine our findings by calculating the critical values R_{Vc} and R_{Hc} required for modeling AABW production off Cape Darnley following Winton et al.'s (1998) hypothesis.

To determine R_{Hc} in the CDP region, we first estimated a depth-plume thickness vertical profile (Fig. 16a) from the 2-km resolution case along the Wild Canyon section shown in Fig. 3. The plume thickness was defined at all points along the slope as the thickness of the layer with $\gamma \geq 28.27 \text{ kg m}^{-3}$ and $\theta < -0.4^\circ \text{ C}$, and data were averaged between day 170 and day 300 to obtain the profile. The profile exhibited two local minima near the shelf break ($H = 171 \text{ m}$ at 300 m depth) and the bottom of the continental slope ($H = 240 \text{ m}$ at 2300 m depth), and a maximum around 1200 m depth ($H = 505 \text{ m}$). This vertical structure is consistent with observations of plume thickness at various points along the slope by Gordon et al. (2009) in the Ross Sea, and the modeled plume thickness of 400 m at 2600 m depth (Fig. 16a) agrees with the observation-based estimate by Ohshima et al. (2013). The general shape of the plume thickness profile followed that of the angle α (Fig. 16b), which varied strongly along the slope. The vertical profile of required R_H (Fig. 16c) showed little variability down to about 1300 m and had a minimum value of 2.1 km at 750 m depth. We can therefore define the critical horizontal resolution in the CDP region as $R_{Hc} = 2.1 \text{ km}$. This value is consistent with the results of our previous analysis suggesting the existence of a 2-km resolution threshold, which validates Winton et al. (1998) hypothesis.

Above the 2-km threshold, excessive warming (Fig. 6c) of the water within the DSW plume likely led to a loss of density, which made the bulk of the dense water stay mid-depth (Fig. 6b). This intermediate water was then advected westward by the ambient current (Fig. 9a–b). Below the 2-km resolution threshold, the properties within the dense water plume were better conserved as colder water reached the slope's bottom (Fig. 6c) through realistic paths (Fig. 8e–f), allowing for AABW to be produced in reasonable amounts (Fig. 6a) and with accurate TS properties (Fig. 13a–b). Minor differences existed in the (1-km vs. 2-km resolution) time series of current velocity (Figs. 10b–c and 11), but this had little influence on AABW properties (Fig. 13a–b).

Our previous analysis suggested that our model in the CDP region was nearly insensitive to vertical resolution (Fig. 7, 14). This is rather unsurprising because the 40-m, 20-m, and 10-m grids all had a vertical resolution much finer than the $R_{Vc} = 85 \text{ m}$ (Table 3) required for this region. However, many models have a vertical grid with depth-varying layer width, such as the ECCO-grid we used in some of our experiments (Table 2). The modeled plume thickness varied between 170 m and 505 m in the CDP region, and a comparison between the plume thickness and the ECCO-grid width (Fig. 16a) shows that even this relatively coarse grid satisfies $R_V \leq H/2$ at all depths above 2000 m.

5.2. Implications for the other AABW formation regions

We estimated the slope steepness α and plume thickness H for the Weddell Sea, the Ross Sea, and the Adelie Coast. We estimated α at all points along the slope from the ETOPO1 global relief model (Amante and Eakins, 2009) by calculating the distance separating the 500 m and 1500 m isobaths. We also provided ranges and an averaged value

Table 3

Plume thickness, slope properties and critical vertical (R_{Vc}) and horizontal (R_{Hc}) for each AABW formation region. $R_{Vc} = H_{\min}/2$. $R_{Hc} = \frac{H}{\alpha}$ based on the assumption that H and α are roughly proportional (See Fig. 16a–b).

Region	Domain	Plume thickness range $H_{\min} - H_{\max}$	Averaged plume thickness (\bar{H})	Averaged slope ($\bar{\alpha}$)	R_{Vc}	R_{Hc}
Cape Darnley Polynya (this study)	Wild Canyon section (Fig. 1)	170–505 m ^a	350 m	0.068	85 m	2.1 km
Ross Sea	170°E–150°W 69.5°S–77.5°S	100–500 m ^b	300 m	0.025	50 m	6.0 km
Weddell Sea	24°W–57°W 68.0°S–75.0°S	200–400 m ^c	300 m	0.020	100 m	7.5 km
Adelie Coast	140°E–149°E 69.5°S–77.5°S	10–447 m ^d	140 m	0.073	25 m ^e	1.0 km

^aThe plume thickness and slope steepness in the CDP region were determined from the model results at 40m2km resolution along the cross section defined in Fig. 1. R_{Hc} for this region was determined following the method described in Section 5.1.

^bThe plume thickness range from the Ross Sea was determined from observations by Budillon et al. (2011), Gordon et al. (2004, 2009), Muench et al. (2009b), Whitworth and Orsi (2006). The mid-range value was taken as the averaged plume thickness.

^cThe plume thickness range from the Weddell Sea was determined from observations by Fahrbach et al. (1995, 2001), Foldvik et al. (2004), Muench and Gordon (1995). The mid-range value was taken as the averaged plume thickness.

^dThe plume thickness range for the Adelie Coast was determined from the minimum and maximum observed plume thickness among 59 CTD profiles listed in Williams et al. (2010). The 59 plume thickness observations were averaged to obtain the 140 m averaged value.

^eAmong the 59 profiles, 49 profiles (83%) had plume thickness equal or greater than 50 m. We used this 50 m value as a reasonable limit for determining R_{Vc} .

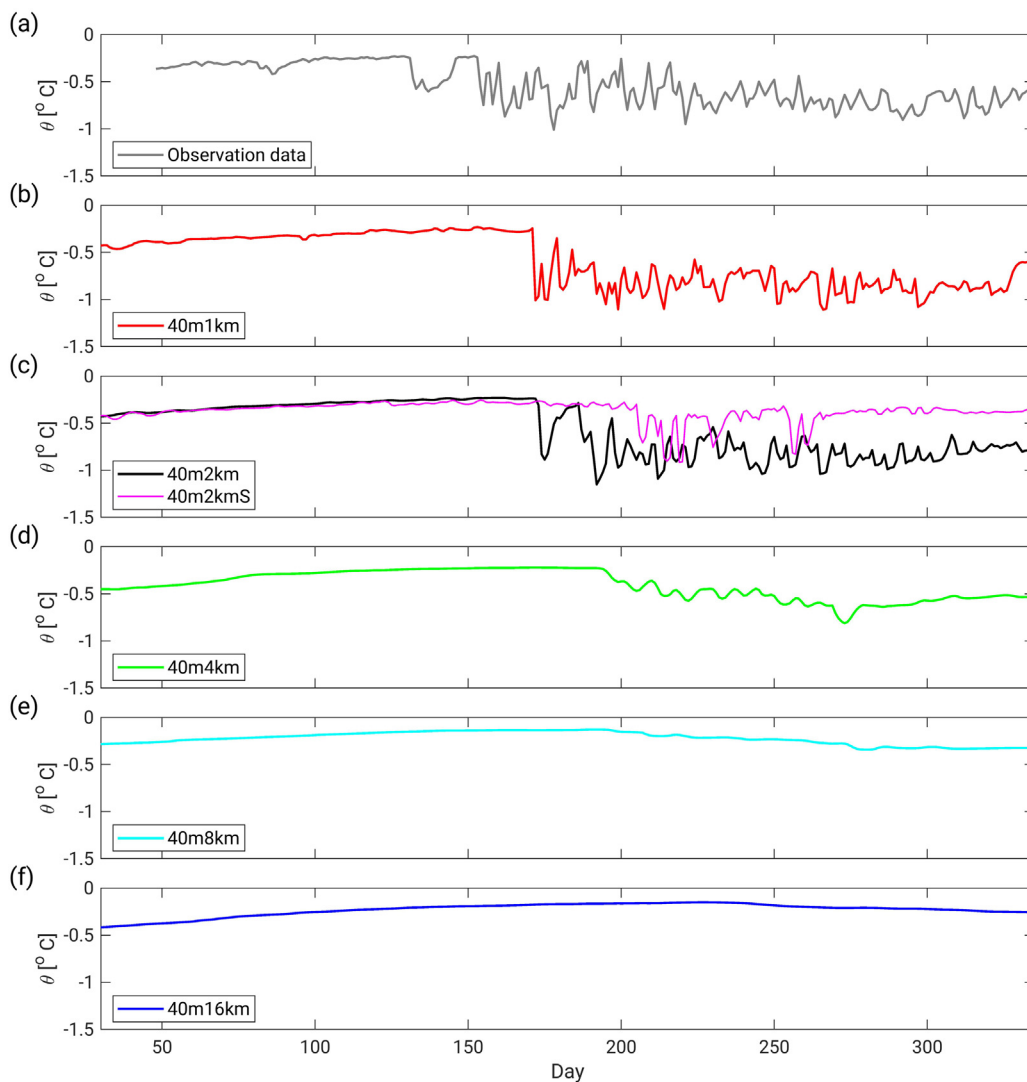


Fig. 12. Time series of bottom temperature at the M3 mooring location from (a) observations, and (b–f) model data for the 40m1km, 40m2km and 40m2kmS, 40m4km, 40m8km, and 40m16km model cases.

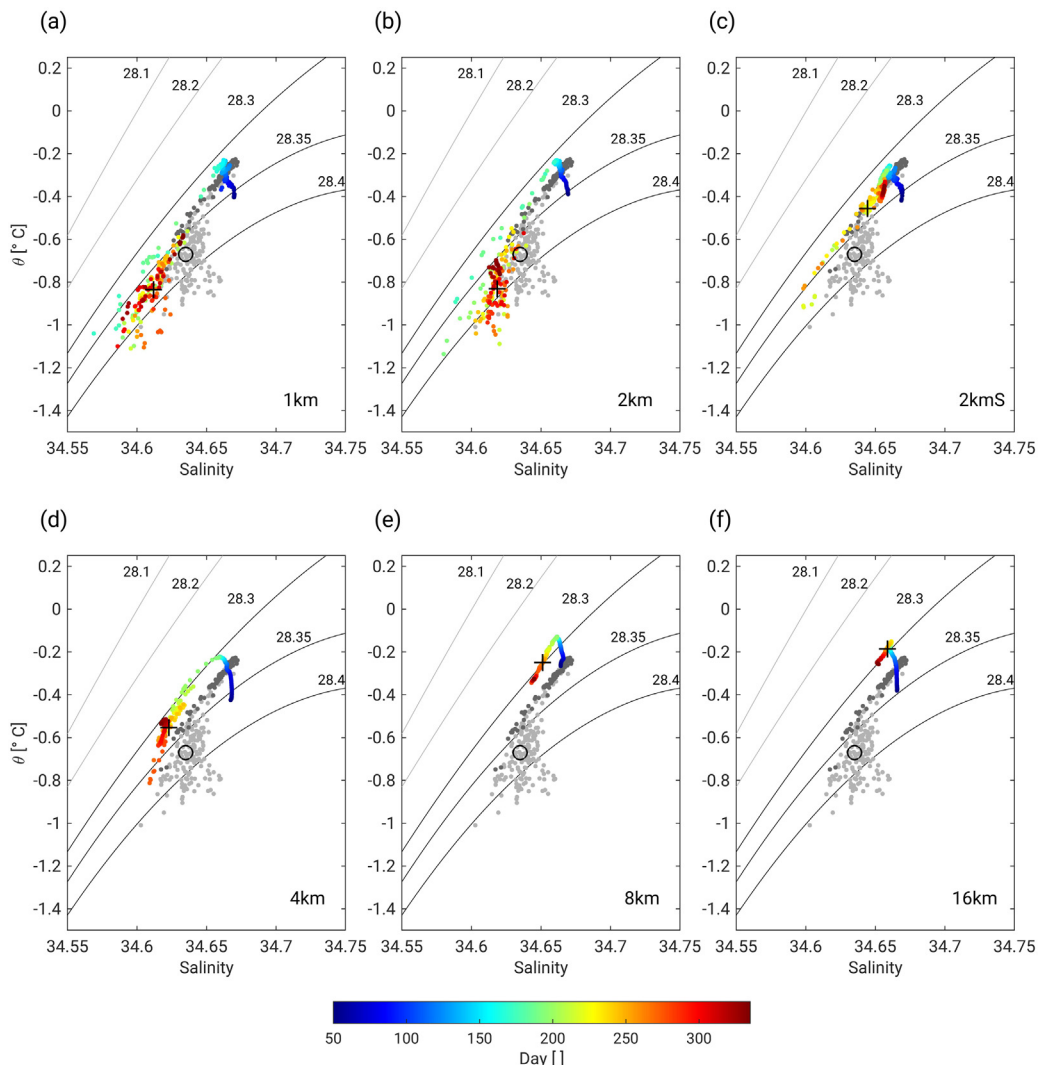


Fig. 13. θ -S diagram of the bottom waters at the M3 mooring for the (a) 40m1km, (b) 40m2km, (c) 40m2kmS, (d) 40m4km, (e) 40m8km, and (f) 40m16km cases. The black crosses in all panels represent the averaged properties between day 200-day 300. The dark and light gray dots in each panel represent the actual θ -S observations at the M3 mooring before and after day 160, respectively. The black circle represent the averaged AABW (CDBW) properties estimated from Ohshima et al. (2013).

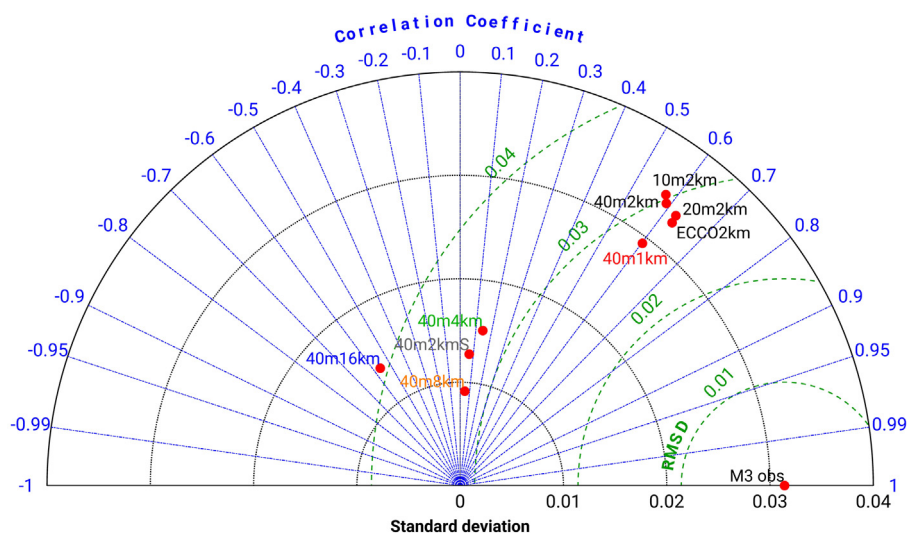


Fig. 14. Taylor diagram listing the statistical properties of the bottom neutral density at M3 from the model cases with different horizontal and vertical resolutions against those of the mooring observations. The radial distances from the center of the semi-circle represent the standard deviation of each time series. The angle represents the correlation coefficient between the observed and modeled daily time series of neutral density. The green dashed curves centered on the “M3 obs” point are a scale for the root mean square differences (between the observed and each modeled time series). The Taylor diagram was drawn using the MATLAB routine taylordiag developed by G. Maze.

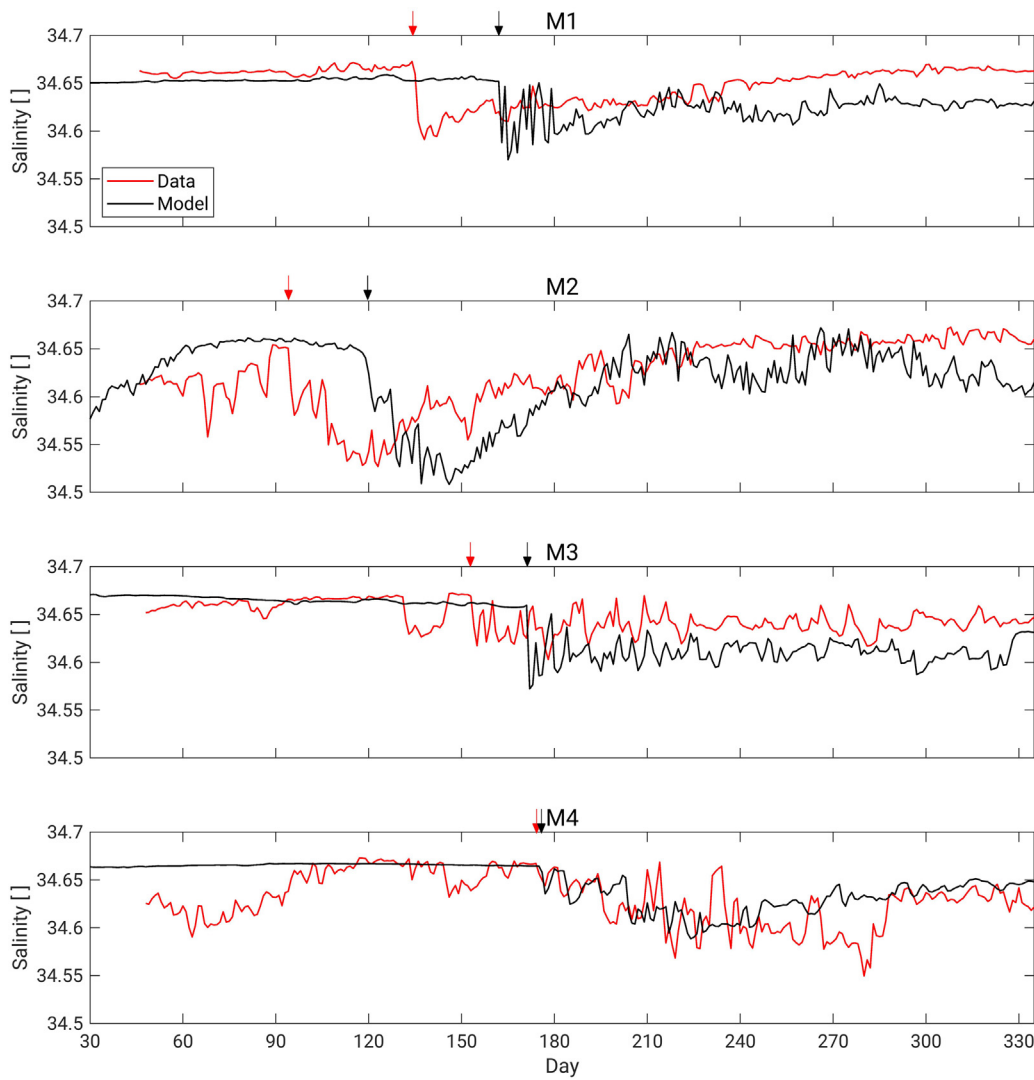


Fig. 15. Time series of bottom salinity at each of the four mooring locations from observations (black solid line) and for the 40m1km model case (red solid line). The black and red arrows mark the date of the first major salinity drop in the data and model, respectively.

of plume thickness for each region, based on observations reported in previous works in Table 3. Averaged values of α and H in the CDP region were also provided for comparison.

The results listed in Table 3 suggest that modeling the Weddell Sea and the Ross Sea would require relatively lower resolutions than in the CDP region due to the weaker slope inclination ($\alpha_{WS} = 0.020$, $\alpha_{RS} = 0.025$) and relatively large plume thickness (300 m on average) in these areas (Table 3). In contrast, properly modeling the AABW formation process off Adelie Land may require higher resolutions due to the high slope inclination ($\alpha = 0.073$) and the thinner plumes ($H_{AC} = 170$ m) observed in this region (Williams et al., 2010).

The lower horizontal resolution required for the Weddell and Ross seas may explain why several models with horizontal resolutions of 3–5 km (Newsom et al., 2016; Morrison et al., 2020) or order (0.1°) (Kerr et al., 2012; Kiss et al., 2020; Renner et al., 2009) yielded relatively realistic DSW pathways and/or estimates of downslope flow volumes or AABW formation rate in one or both of these seas. In particular, the densest bottom waters in Newsom et al.'s (2016) high-resolution Community Climate System Model (grid spacing 3–5 km) were found in the Ross Sea and the Weddell Sea, which implies that the resolution of that model was sufficient for these areas. On the other hand, the model by Kusahara et al. (2010) yielded realistic DSW production and pathways with horizontal resolution ranging between

"a few kilometers and 15-km" in East Antarctica, but could not reproduce well the mixing process of the downsloping DSW. This may be explained by the 2.1-km R_{Hc} for the CDP region being smaller than the resolution of this model.

6. Summary and conclusion

AABW is an essential ocean water mass that plays a crucial role in the global thermohaline circulation. However, modeling the formation and downslope descent of DSW and AABW production is challenging. In this study, sensitivity tests with different vertical and horizontal resolutions were conducted to assess how resolution impacts DSW production and its downslope flow off the CDP.

The essential criterion controlling downslope flow was horizontal resolution. For resolutions equal to or higher than a 2-km threshold, the simulations yielded realistic downslope flow, AABW properties, and bottom current and hydrographic properties variability, all consistent with observations in the region (Ohshima et al., 2013). The processes leading to the formation and downslope flow in the CDP were properly captured by the model, especially the periodic, high-frequency variability of the downslope flow in the Wild Canyon (Nakayama et al., 2014; Ohshima et al., 2013). Considering the continental slope angle and plume thickness in the CDP region, the 2-km threshold we found

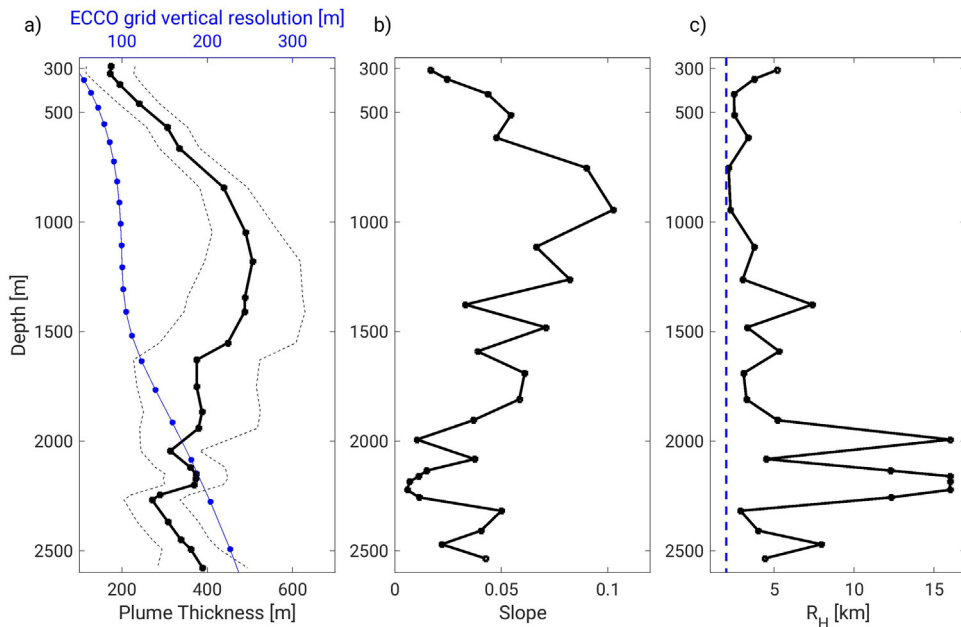


Fig. 16. (a) Profiles of (a) time averaged (day 170 to day 300) plume thickness H (black) and ECCO grid vertical resolution (blue), (b) slope angle α , and (c) minimum required horizontal resolution R_H calculated following Winton et al. (1998) as $(H/2)/\alpha$ (see Section 5.1). The dashed line in (c) represents the 2-km threshold suggested by our previous results, and the critical horizontal resolution R_{Hc} is the minimum R_H value in the profile, i.e. 2.1-km at 750 m depth. In (a), the ECCO grid vertical resolution becomes insufficient to fully resolve the plume after the blue line crosses the black line.

was consistent with Winton et al.'s (1998) hypothesis that horizontal resolution depends on these two parameters. For resolutions lower than 2-km, the comparison between model outputs and observations worsened with decreasing resolution. For example, at 4-km resolution, the downslope flow was reduced by 20% compared to the 1-km and 2-km resolution, and at 16-km resolution, AABW density was strongly underestimated. Our results suggest that as the resolution was decreased, increasing amounts of intermediate water were formed and advected westward, to the detriment of AABW formation.

Further, we demonstrated that a bathymetric dataset with poor data density produced AABW with misestimated properties, even at high horizontal resolutions. When a 16-km resolution bathymetry was linearly interpolated to the 2-km resolution grid, the downslope flow of DSW and properties of AABW were largely underestimated, similar to the 4-km resolution results. Acquiring a high-resolution bathymetric dataset in the four regions where AABW is formed is therefore essential to properly model bottom water formation in the polar regions.

Our model results were mostly insensitive to vertical resolution because in most of the vertical grids tested, the grid width was much smaller than half the plume thickness (Winton et al., 1998). Even with a coarse vertical grid, such as that of the ECCO state estimate (~170 m wide at ~2000 m), a model with a fine horizontal resolution can reproduce the downslope flow of DSW and its volume in the CDP region, as well as the main AABW characteristics. Our results suggest that coupled ice-ocean models with a similar configuration as ours may properly model the formation and properties of AABW in other polynya regions of the world's oceans. However, as plume thickness and slope angle affect the resolutions needed to resolve the downslope flows, differences in the resolutions required in the different AABW formation regions may exist.

Sensitivity experiments conducted in this study clarified the crucial role of resolution and fine-scale bathymetry for generating the downslope flow of DSW, its pathways, and the formation of AABW with properties close to observations. While regional models can be conducted at high resolutions (higher than 2 km) at a reasonable computational cost, global circulation models have to employ coarser resolutions. Parametrisation of topographic properties in these coarse resolution models is an essential matter (e.g., Matsumura and Hasumi,

2011), and our study is a step towards addressing this issue. Also, while we found that resolutions of order (10 km) are inadequate to model AABW formation, parametrisation of the bottom boundary layer processes may enable to solve the issue of excessive convective mixing (Wang et al., 2008; Winton et al., 1998) affecting models at these resolutions. The development or improvement of such parametrisation is a topic that remains for future studies.

CRediT authorship contribution statement

Vigan Mensah: Conceptualization, Methodology, Validation, Formal analysis, Investigation, Original draft, Reviewing and editing, Visualization. **Yoshihiro Nakayama:** Conceptualization, Methodology, Software, Reviewing and editing, Supervision, Funding acquisition, Project administration. **Masakazu Fujii:** Resources, Software. **Yoshifumi Nogi:** Resources. **Kay I. Ohshima:** Reviewing and editing, Supervision, Funding acquisition, Project administration.

Declaration of competing interest

The authors declare that they have no known competing financial interests or personal relationships that could have appeared to influence the work reported in this paper.

Acknowledgments

This study was supported by the Cooperative Research Activities of Collaborative Use of Computing Facility of the Atmosphere and Ocean Research Institute, The University of Tokyo. The mooring observation data used in the model-data comparisons were processed by Y. Fukamachi. We are grateful to two anonymous reviewers, whose comments greatly contributed to improving the quality of this paper. We extend our thanks to the editor for this paper, H. Hasumi.

This work was supported by Grants-in-Aid for Scientific Research #17H01157, 17H06317, 20H05707, and 21K13989 from the Ministry of Education, Culture, Sports, Science and Technology of Japan.

The marine mammal data were collected and made freely available by the International MEOP Consortium and the national programs

that contribute to it. (<http://www.meop.net>). Argo float data collected and made freely available by the International Argo Program and the national programs that contribute to it. (<https://argo.ucsd.edu>, <https://www.ocean-ops.org>). The Argo Program is part of the Global Ocean Observing System. Argo float data were downloaded together with other historical CTD data as part of the World Ocean Database 2018, a *National Centers for Environmental Information* standard product. Data analyses were conducted using the Pan-Okhotsk Information System of Hokkaido University.

The MITgcm 3d ocean model used for this work is a community-developed model available for download from http://mitgcm.org/public/source_code.html. The code and input files for running the 40-m vertical_2-km horizontal resolution experiment, 40-m vertical_1-km horizontal resolution experiment, and the complete set of model outputs for the 40-m vertical_2-km horizontal resolution are archived in Zenodo, a public, community-supported repository, at <https://doi.org/10.5281/zenodo.4898376>. These codes are publicly available, with no restrictions.

References

- Abrahamsen, E.P., Meijers, A.J., Polzin, K.L., Garabato, A.C.N., King, B.A., Firing, Y.L., Meredith, M.P., 2019. Stabilization of dense Antarctic water supply to the Atlantic Ocean overturning circulation. *Nature Clim. Change* 9 (10), 742–746.
- Aldcroft, A., Hill, C., Marshall, J., 1997. Representation of topography by shaved cells in a height coordinate ocean model. *Mon. Weather Rev.* 125, 2293–2315. [http://dx.doi.org/10.1175/1520-0493\(1997\)125<2293:ROTBSC>2.0.CO;2](http://dx.doi.org/10.1175/1520-0493(1997)125<2293:ROTBSC>2.0.CO;2).
- Amante, C., Eakins, B.W., 2009. ETOP01 1 arc-minute global relief model: Procedures, data sources and analysis. In: NOAA Technical Memorandum NESDIS NGDC-24. National Geophysical Data Center, NOAA., <http://dx.doi.org/10.7289/V5C8276M>.
- Aoki, S., Ono, K., Hirano, D., et al., 2020. Continuous winter oceanic profiling in the Cape Darnley Polynya, East Antarctica. *J. Oceanogr.* 76, 365–372. <http://dx.doi.org/10.1007/s10872-020-00550-w>.
- Azaneu, M., Kerr, R., Mata, M.M., 2014. Assessment of the representation of Antarctic bottom water properties in the ECCO2 reanalysis. *Ocean Sci.* 10, 923–946. <http://dx.doi.org/10.5194/os-10-923-2014>.
- Baines, P.G., Condie, S., 1998. Observations and modelling of antarctic downslope flows: A review. In: Jacobs, S.S., Weiss, R.F. (Eds.), *Ocean, Ice, and Atmosphere: Interactions at the Antarctic Continental Margin*. In: *Antarctic Research Series*, vol. 75, AGU, Washington DC, pp. 29–49.
- Bindoff, N.L., Rintoul, S.R., Massom, R., 2000. Bottom water formation and polynyas in Adélie Land, Antarctica. *Pap. Proc. R. Soc. Tasmania* 133 (3), 51–56.
- Boyer, T.P., Baranova, O.K., Coleman, C., Garcia, H.E., Grodsky, A., Locarnini, R.A., Mishonov, A.V., O'Brien, T.D., Paver, C.R., Reagan, J.R., Seidov, D., Smolyar, I.V., Weathers, K., Zweng, M.M., 2018. World ocean database 2018. In: NCEI StandArd Product: World Ocean Database (WOD). NOAA National Centers for Environmental Information. Dataset.
- Budillon, G., Castagno, P., Aliani, S., Spezie, G., Padman, L., 2011. Thermohaline variability and Antarctic bottom water formation at the ross sea shelf break. *Deep Sea Res. Part I* 58, 1002–1018.
- Carton, J.A., Giese, B., 2008. A reanalysis of ocean climate using simple ocean data assimilation (SODA). *Mon. Weather Rev.* 136, 2999–3017.
- Dotto, T.S., Kerr, R., Mata, M.M., Azaneu, M., Wainer, I.E.K.C., Fahrbach, E., Rohardt, G., 2014. Assessment of the structure and variability of Weddell sea water masses in distinct ocean reanalysis products. *Ocean Sci.* 10, 523–546.
- Downes, S.M., Gnanadesikan, A., Griffies, S.M., Sarmiento, J.L., 2011. Water mass exchange in the southern ocean in coupled climate models. *J. Phys. Oceanogr.* 41, 1756–1771. <http://dx.doi.org/10.1175/2011JPO4586.1>.
- Dutay, J.-C., Bullister, J.L., Doney, S.C., Orr, J.C., Najjar, R., Caldeira, K., et al., 2002. Evaluation of ocean model ventilation with CFC-11: Comparison of 13 global ocean models. *Ocean Model.* 4 (2), 89–120. [http://dx.doi.org/10.1016/S1463-5003\(01\)00013-0](http://dx.doi.org/10.1016/S1463-5003(01)00013-0).
- ECCO Consortium, Fukumori, I., Wang, O., Fenty, I., Forget, G., Heimbach, P., Ponte, R.M., 2019. ECCO central estimate (version 4 release 4). Retrieved from <https://eccō.jpl.nasa.gov/drive/files>.
- ECCO Consortium, Fukumori, I., Wang, O., Fenty, I., Forget, G., Heimbach, P., Ponte, R.M., 2021. Synopsis of the ECCO central production global ocean and sea-ice state estimate (version 4 release 4). <http://dx.doi.org/10.5281/zenodo.4533349>.
- England, M.H., 1992. On the formation of Antarctic intermediate and bottom water in ocean general circulation models. *J. Phys. Oceanogr.* 22, 918–926. [http://dx.doi.org/10.1175/1520-0485\(1992\)022<0918:OTFOAI>2.0.CO;2](http://dx.doi.org/10.1175/1520-0485(1992)022<0918:OTFOAI>2.0.CO;2).
- Fahrbach, E., Harms, S., Rohardt, G., Schröder, M., Woodgate, R.A., 2001. Flow of bottom water in the northwestern Weddell sea. *J. Geophys. Res.* 106 (C2), 2761–2778. <http://dx.doi.org/10.1029/2000JC00142>.
- Fahrbach, E., Rohardt, G., Scheele, N., Schröder, M., Strass, V., Wisotzki, A., 1995. Formation and discharge of deep and bottom water in the northwestern Weddell sea. *J. Mar. Res.* 53, 515–538.
- Ferreira, M.L., Kerr, R., 2017. Source water distribution and quantification of North Atlantic deep water and Antarctic bottom water in the Atlantic Ocean. *Prog. Oceanogr.* 153, 66–83.
- Foldvik, A., Gammelsrød, T., Østerhus, S., Fahrbach, E., Rohardt, G., Schröder, M., Nicholls, K.W., Padman, L., Woodgate, R.A., 2004. Ice shelf water overflow and bottom water formation in the southern Weddell sea. *J. Geophys. Res.* 109, C02015. <http://dx.doi.org/10.1029/2003JC002008>.
- Foldvik, A., Gammelsrød, T., Tørresen, T., 1985. Circulation and water masses on the southern Weddell sea shelf. *Oceanol. Antarct. Cont. Shelf* 5–20.
- Foster, T.D., Carmack, E.C., 1976. Frontal zone mixing and Antarctic bottom water formation in the southern Weddell sea. *Deep Sea Res. Oceanogr. Abstr.* 23 (4), 301–317.
- Fraser, A.D., Massom, R.A., Ohshima, K.I., Willmes, S., Kappes, P.J., Cartwright, J., Porter-Smith, R., 2020. High-resolution mapping of circum-Antarctic landfast sea ice distribution, 2000–2018. *Earth Syst. Sci. Data* 12, 2987–2999. <http://dx.doi.org/10.5194/essd-12-2987-2020>.
- Fraser, A.D., Ohshima, K.I., Nihashi, S., Massom, R.A., Tamura, T., Nakata, K., Williams, G.D., Carpenterier, S., Willmes, S., 2019. Landfast ice controls on sea-ice production in the Cape Darnley Polynya: A case study. *Remote Sens. Environ.* 233, 111315. <http://dx.doi.org/10.1016/j.rse.2019.111315>.
- Fukamachi, Y., Wakatsuchi, M., Taira, K., Kitagawa, S., Ushio, S., Takahashi, A., Oikawa, K., Furukawa, T., Yoritaka, H., Fukuchi, M., Yamamoto, T., 2000. Seasonal variability of bottom water properties off Adelie Land, Antarctica. *J. Geophys. Res.* 105, 6531–6540.
- Gill, A., 1973. Circulation and bottom water production in the Weddell sea. *Deep Sea Res. Oceanogr. Abstr.* 20 (2), 111–140.
- Goosse, H., Campin, J.M., Tartinville, B., 2001. The sources of Antarctic bottom water in a global ice-ocean model. *Ocean Model.* 3 (1–2), 51–65.
- Gordon, A.L., Huber, B.A., Hellmer, H.H., Field, A., 1993. Deep and bottom water of the Weddell sea's western rim. *Science* 262, 95–97.
- Gordon, A.L., Orsi, A.H., Muensch, R., Huber, B.A., Zambianchi, E., Visbeck, M., 2009. Western Ross sea continental slope gravity currents. *Deep Sea Res. Part II* 56 (13–14).
- Gordon, A.L., Zambianchi, E., Orsi, A., Visbeck, M., Giulivi, C.F., Whitworth, T., Spezie, G., 2004. Energetic plumes over the western Ross sea continental slope. *Geophys. Res. Lett.* 31, L21302. <http://dx.doi.org/10.1029/2004GL020785>.
- Heuzé, C., Heywood, K.J., Stevens, D.P., Ridley, J.K., 2013. Southern ocean bottom water characteristics in CMIP5 models. *Geophys. Res. Lett.* 40 (7), 1409–1414.
- Hirano, D., Kitade, Y., Ohshima, K.I., Fukamachi, Y., 2015. The role of turbulent mixing in the modified shelf water overflows that produce Cape Darnley bottom water. *J. Geophys. Res. Oceans* 120, 910–922. <http://dx.doi.org/10.1002/2014JC010059>.
- Jacobs, S.S., Amos, A.F., Bruchhausen, P.M., 1970. Ross sea oceanography and Antarctic bottom water formation. *Deep-Sea Res. Oceanogr. Abstr.* 17, 935–970.
- Johnson, G.C., 2008. Quantifying Antarctic bottom water and north Atlantic deep water volumes. *J. Geophys. Res.* 113, C05027. <http://dx.doi.org/10.1029/2007JC004477>.
- Kerr, R., Dotto, T.S., Mata, M.M., Hellmer, H.H., 2018. Three decades of deep water mass investigation in the Weddell sea (1984–2014): temporal variability and changes. *Deep Sea Res. Part II* 149, 70–83.
- Kerr, R., Heywood, K.J., Mata, M.M., Garcia, C.A.E., 2012. On the outflow of dense water from the Weddell and Ross seas in OCCAM model. *Ocean Sci.* 8 (3), 369–388. <http://dx.doi.org/10.5194/os-8-369-2012>.
- Kerr, R., Wainer, I., Mata, M.M., 2009. Representation of the Weddell sea deep water masses in the ocean component of the NCAR–CCSM model. *Antarct. Sci.* 21 (3), 301.
- Kim, S.-J., Stossel, A., 1998. On the representation of the southern ocean water masses in an ocean climate model. *J. Geophys. Res.* 103 (C11), 24891–24906.
- Kiss, A.E., Hogg, A., McC, N., Boeira Dias, F., Brassington, G.B., Chamberlain, M.A., Chapman, C., Dobrohotoff, P., Domingues, C.M., Duran, E.R., England, M.H., Fiedler, R., Griffies, S.M., Heerdegen, A., Heil, P., Holmes, R.M., Klocker, A., Marsland, S.J., Morrison, A.K., Munroe, J., Nikurashin, M., Oke, P.R., Pilo, G.S., Richet, O., Savita, A., Spence, P., Stewart, K.D., Ward, M.L., Wu, F., Zhang, X., 2020. ACCESS–OM2 v1.0: A global ocean-sea ice model at three resolutions. *Geosci. Model Dev.* 13, 401–442.
- Kusahara, K., Hasumi, H., Tamura, T., 2010. Modeling sea ice production and dense water formation in coastal polynyas around east Antarctica. *J. Geophys. Res.* 115, C10006. <http://dx.doi.org/10.1029/2010JC006133>.
- Kusahara, K., Williams, G.D., Tamura, T., Massom, R., Hasumi, H., 2017. Dense shelf water spreading from Antarctic coastal polynyas to the deep southern ocean: A regional circumpolar model study. *J. Geophys. Res.* 122, <http://dx.doi.org/10.1002/2017JC012911>.
- Losch, M., Menemenlis, D., Campin, J.M., Heimbach, P., Hill, C., 2010. On the formulation of sea-ice models: Part 1: Effects of different solver implementations and parameterizations. *Ocean Mod.* 33, 129–144. <http://dx.doi.org/10.1016/j.ocemod.2009.12.008>, doi: 790.
- Lumpkin, R., Speer, K., 2007. Global ocean meridional overturning. *J. Phys. Oceanogr.* 37, 2550–2562. <http://dx.doi.org/10.1175/JPO3130.1>.

- Markus, T., Kottmeier, C., Fahrbach, E., 1998. Ice formation in coastal polynyas in the Weddell sea and their impact on oceanic salinity. In: Jeffries, M.O. (Ed.), Antarctic Sea Ice: Physical Processes, Interactions and Variability. In: *Antarct. Res. Ser.*, vol. 74, AGU, Washington, D.C., pp. 273–292.
- Marshall, J., Adcroft, A., Hill, C., Perelman, L., Heisey, C., 1997. J. Geophys. Res. Oceans 102 (C3), 5753–5766, https://en.wikipedia.org/wiki/Journal_of_Geophysical_Research:_Oceans.
- Matsumura, Y., Hasumi, H., 2010. Modeling ice shelf water overflow and bottom water formation in the southern Weddell sea. J. Geophys. Res. 115, C10033. <http://dx.doi.org/10.1029/2009JC005841>.
- Matsumura, Y., Hasumi, H., 2011. Dynamics of cross-isobath dense water transport induced by slope topography. J. Phys. Oceanogr. 41, 2402–2416. <http://dx.doi.org/10.1175/JPO-D-10-05014.1>.
- Mazloff, M.R., Heimbach, P., Wunsch, C., 2010. An eddy-permitting southern ocean state estimate. J. Phys. Oceanogr. 40, 880–899.
- Morales Maqueda, M.A., Willmott, A.J., Biggs, N.R.T., 2004. Polynya dynamics: A review of observations and modeling. Rev. Geophys. 42, RG1004. <http://dx.doi.org/10.1029/2002RG000116>.
- Morrison, A.K., Hogg, A.M.C.C., England, M.H., Spence, P., 2020. Warm circumpolar deep water transport toward Antarctica driven by local dense water export in canyons. Sci. Adv. 6 (18), <http://dx.doi.org/10.1126/sciadv.aav2516>.
- Muench, R.D., Gordon, A.L., 1995. Circulation and transport of water along the western Weddell sea margin. J. Geophys. Res. 100, 18503–18515.
- Muench, R., Padman, L., Gordon, A., Orsi, A., 2009b. A dense water outflow from the ross sea, antarctica: mixing and the contribution of tides. J. Mar. Syst. 77 (4), 369–387.
- Muench, R., Wählén, A., Özgökmen, T., Hallberg, R., Padman, L., 2009a. Impacts of bottom corrugations on a dense Antarctic outflow: the NW Ross sea. Geophys. Res. Lett. 36, 23. <http://dx.doi.org/10.1029/2009GL041347>.
- Nakata, K., Ohshima, K.I., Nihashi, S., 2019. Estimation of thin-ice thickness and discrimination of ice type from AMSR-E passive microwave data. IEEE Trans. Geosci. Remote Sens. 57 (1), 263–276. <http://dx.doi.org/10.1109/TGRS.2018.2853590>.
- Nakata, K., Ohshima, K.I., Nihashi, S., 2021. Mapping of active frazil for Antarctic coastal polynyas, with an estimation of sea-ice production. Geophys. Res. Lett. 48, <http://dx.doi.org/10.1029/2020GL091353>, e2020GL091353.
- Nakayama, Y., Menemenlis, D., Zhang, H., et al., 2018. Origin of circumpolar deep water intruding onto the Amundsen and Bellingshausen sea continental shelves. Nature Commun. 9, 3403. <http://dx.doi.org/10.1038/s41467-018-05813-1>.
- Nakayama, Y., Ohshima, K.I., Matsumura, Y., Fukamachi, Y., Hasumi, H., 2014. A numerical investigation of formation and variability of Antarctic bottom water off Cape Darnley, East Antarctica. J. Phys. Oceanogr. 44, 2921–2937. <http://dx.doi.org/10.1175/JPO-D-14-0069.1>.
- Newsom, E.R., Bitz, C.M., Bryan, F.O., Abernathy, R., Gent, P.R., 2016. Southern ocean deep circulation and heat uptake in a high-resolution climate model. J. Clim. 29, 2597–2619. <http://dx.doi.org/10.1175/JCLI-D-15-0513.1>.
- Nicholls, K.W., Østerhus, S., Makinson, K., Gammelsrød, T., Fahrbach, E., 2009. Ice-ocean processes over the continental shelf of the southern Weddell sea, Antarctica: A review. Rev. Geophys. 47 (3).
- Nihashi, S., Ohshima, K.I., 2015. Circumpolar mapping of Antarctic coastal polynyas and landfast sea ice: Relationship and variability. J. Clim. 28, 3650–3670. <http://dx.doi.org/10.1175/JCLI-D-14-00369.1>.
- Ohshima, K.I., Fukamachi, Y., Williams, G.D., Nihashi, S., Roquet, F., Kitade, Y., Tamura, T., Hirano, D., Herranz-Borreguero, L., Field, I., Hindell, M., Aoki, S., Wakatsuchi, M., 2013. Antarctic bottom water production by intense sea-ice formation in the Cape Darnley polynya. Nat. Geosci. 6 (3), 235–240.
- Orsi, A.H., Johnson, G.C., Bullister, J.L., 1999. Circulation, mixing, and production of Antarctic bottom water. Prog. Oceanogr. 43, 55–109.
- Orsi, A.H., Wiederwohl, C.L., 2009. A recount of Ross sea waters. Deep-Sea Res. II 56, 778–795.
- Purkey, S.G., Johnson, G.C., 2010. Warming of global abyssal and deep southern ocean waters between the 1990s and 2000s: contributions to global heat and sea level rise budgets. J. Clim. 23 (23), 6336–6351.
- Purkey, S.G., Johnson, G.C., 2013. Antarctic bottom water warming and freshening: contributions to sea level rise, ocean freshwater budgets, and global heat gain. J. Clim. 26 (16), 6105–6122.
- Renfrew, I.A., King, J.C., Markus, T., 2002. Coastal polynyas in the southern Weddell sea: Variability of the surface energy budget. J. Geophys. Res. 107 (C6), 3063. <http://dx.doi.org/10.1029/2000JC000720>.
- Renner, A.H., Heywood, K.J., Thorpe, S.E., 2009. Validation of three global ocean models in the Weddell sea. Ocean Model. 30 (1), 1–15.
- Rintoul, S., 1998. On the origin and influence of Adélie land bottom water. In: Jacobs, S.S., Weiss, R.F. (Eds.), *Ocean, Ice and Atmosphere: Interactions at the Antarctic Continental Margin*. In: *Antarct. Res. Ser.*, vol. 75, AGU, Washington, D.C., pp. 151–172.
- Rodehacke, C.B., Hellmer, H.H., Beckmann, A., Roether, W., 2007. Formation and spreading of Antarctic deep and bottom waters inferred from a chlorofluorocarbon (CFC) simulation. J. Geophys. Res. 112, C09001. <http://dx.doi.org/10.1029/2006JC003884>.
- Rodman, M., Gordon, A.L., 1982. Southern ocean bottom water of the Australian-New Zealand sector. J. Geophys. Res. 87, 5771–5778.
- Sasai, Y., Ishida, A., Yamanaka, Y., Sasaki, H., 2004. Chlorofluorocarbons in a global ocean eddy-resolving OGCM: Pathways and formation of Antarctic bottom water. Geophys. Res. Lett. 31, L12305. <http://dx.doi.org/10.1029/2004GL019895>.
- Schmitz, J.W.J., 1995. On the interbasin-scale thermohaline circulation. Rev. Geophys. 33, 151–173.
- Shimada, K., Aoki, S., Ohshima, K.I., 2017. Creation of a gridded dataset for the southern ocean with a topographic constraint scheme. J. Atmos. Ocean. Technol. 34, 511–532. <http://dx.doi.org/10.1175/JTECH-D-16-0075>.
- Snow, K., Hogg, A.M., Sloyan, B.M., Downes, S.M., 2016. Sensitivity of Antarctic bottom water to changes in surface buoyancy fluxes. J. Clim. 29, 313–330. <http://dx.doi.org/10.1175/JCLI-D-15-0467.1>.
- Stössel, A., Kim, S., Drijfhout, S.S., 1998. The impact of southern ocean sea ice in a global ocean model. J. Phys. Oceanogr. 28, 1999–2018. [http://dx.doi.org/10.1175/1520-0485\(1998\)028<1999:TIOS>2.0.CO;2](http://dx.doi.org/10.1175/1520-0485(1998)028<1999:TIOS>2.0.CO;2).
- Talley, L., 2013. Closure of the global overturning circulation through the indian, pacific, and southern oceans: Schematics and transports. Oceanography 26 (1), 80–97.
- Tamura, T., Ohshima, K.I., Fraser, A.D., Williams, G.D., 2016. Sea ice production variability in Antarctic coastal polynyas. J. Geophys. Res. Oceans 121, 2967–2979. <http://dx.doi.org/10.1002/2015JC011537>.
- Taylor, K.E., 2001. Summarizing multiple aspects of model performance in a single diagram. J. Geophys. Res. 106 (D7), 7183–7192. <http://dx.doi.org/10.1029/2000JD900719>.
- Treasure, A., Roquet, F., Ansorge, J.I., Bester, M., Boehme, L., 2017. Marine mammals exploring the oceans pole to pole: A review of the MEOP consortium. Oceanography 30, 132–138. <http://dx.doi.org/10.5670/oceanog.2017.234>.
- Treguier, A.M., Sommer, J.L., Molines, J.M., de Cuevas, B., 2010. Response of the southern ocean to the southern annular mode: interannual variability and multidecadal trend. J. Phys. Oceanogr. 40, 1659–1668.
- Van Sebille, E., Spence, P., Mazloff, M.R., England, M.H., Rintoul, S.R., Saenko, O.A., 2013. Abyssal connections of Antarctic bottom water in a southern ocean state estimate. Geophys. Res. Lett. 40, 2177–2182. <http://dx.doi.org/10.1002/grl.50483>.
- Wang, Q., Danilov, S., Schröter, J., 2008. Comparison of overflow simulations on different vertical grids using the finite element ocean circulation model. Ocean Model. 20 (4), 313–335. <http://dx.doi.org/10.1016/j.ocemod.2007.10.005>.
- Wessel, P., Smith, W.H.F., Scharroo, R., Luis, J., Wobbe, F., 2013. Generic mapping tools: Improved version released. Eos Trans. AGU 94 (45), 409.
- Whitworth, T., III, Orsi, A.H., 2006. Antarctic bottom water production and export by tides in the Ross sea. Geophys. Res. Lett. 33, L12609.
- Whitworth III, T., Orsi, A.H., Kim, S.-J., Nowlin Jr., W.D., 1998. Water masses and mixing near the Antarctic slope front. In: Jacobs, S.S., Weiss, R.F. (Eds.), *Ocean, Ice, and Atmosphere: Interactions at the Antarctic Continental Margin*. In: *Antarctic Research Series*, Amer. Geophys. Union, pp. 1–27.
- Williams, G.D., Aoki, S., Jacobs, S.S., Rintoul, S.R., Tamura, T., Bindoff, N.L., 2010. Antarctic bottom water from the Adelie and George V Land coast, east Antarctica (140–149°E). J. Geophys. Res. 115 (C04027), 29. <http://dx.doi.org/10.1029/2009JC005812>.
- Williams, G.D., Herranz-Borreguero, L., Roquet, F., Tamura, T., Ohshima, K.I., Fukamachi, Y., Fraser, A.D., Gao, L., Chen, H., McMahon, C.R., Harcourt, R., Hindell, M., 2016. The suppression of Antarctic bottom water formation by melting ice shelves in prydz bay. Nat. Comm. 7 (12577), <http://dx.doi.org/10.1038/ncomms12577>.
- Winton, M., Hallberg, R., Gnanadesikan, A., 1998. Simulation of density-driven frictional downslope flow in Z-coordinate ocean models. J. Phys. Oceanogr. 28 (11), 2163–2174.
- Wong, A., Riser, S., 2011. Profiling float observations of the upper ocean under sea ice off the Wilkes land coast of Antarctica. J. Phys. Oceanogr. 41, 1102–1115.
- Zhang, H., Menemenlis, D., Fenty, I., 2018. ECCO LLC270 ocean-ice state estimate. available at <https://dspace.mit.edu/handle/1721.1/119821>.